https://doi.org/10.5194/egusphere-2024-410
Preprint. Discussion started: 29 February 2024

Enhancing Long-Term Trend Simulation of Global Tropospheric OH and Its Drivers from 2005-2019: A Synergistic Integration of Model Simulations and Satellite Observations

Amir H. Souri[1,2*], Bryan N. Duncan[1], Sarah A. Strode[1,2], Daniel C. Anderson[1,3], Michael E. Manyin[1,4], Junhua Liu[1,2], Luke D. Oman[1], Zhen Zhang[5,6], and Brad Weir[2,7]

[1]Atmospheric Chemistry and Dynamics Laboratory, NASA Goddard Space Flight Center (GSFC), Greenbelt, MD, USA
[2]GESTAR II, Morgan State University, Baltimore, MD, USA
[3]GESTAR II, University of Maryland Baltimore County, Baltimore, MD, USA
[4]Science Systems and Applications, Inc., Lanham, MD, USA
[5]National Tibetan Plateau Data Center (TPDC), State Key Laboratory of Tibetan Plateau Earth System, Environment and Resource (TPESER), Institute of Tibetan Plateau Research, Chinese Academy of Sciences, Beijing, China
[6]Earth System Science Interdisciplinary Center, University of Maryland, College Park, MD, USA
[7]NASA Global Modeling and Assimilation Office (GMAO), Goddard Space Flight Center, Greenbelt, MD, USA

* Corresponding author: a.souri@nasa.gov

https://doi.org/10.5194/egusphere-2024-410
Preprint. Discussion started: 29 February 2024

Abstract

The tropospheric hydroxyl radical (TOH) is a key player in regulating oxidation of various compounds in Earth's atmosphere. Despite its pivotal role, the spatiotemporal distributions of OH are poorly constrained. Past modeling studies suggest that the main drivers of OH, including NO_2, tropospheric ozone (TO_3), and H_2O(v), have increased TOH globally. However, these findings often offer a global average and may not include more recent changes in diverse compounds emitted on various spatiotemporal scales. Here, we aim to deepen our understanding of global TOH trends for more recent years (2005-2019) at 1×1 degrees. To achieve this, we use satellite observations of HCHO and NO_2 to constrain simulated TOH using a technique based on a Bayesian data fusion method, alongside an interpretable machine learning module named ECCOH, which is integrated into NASA's GEOS global model. This innovative module helps efficiently predict the convoluted response of TOH to its drivers/proxies. Aura Ozone Monitoring Instrument (OMI) NO_2 observations suggest that the simulation has high biases over biomass burning activities in Africa and Eastern Europe, resulting in overestimation of up to 20% in TOH, regionally. OMI HCHO primarily impacts oceans where TOH linearly correlates with this proxy. Five key parameters including TO_3, H_2O(v), NO_2, HCHO, and stratospheric ozone can collectively explain 65% of variance in TOH trends. The overall trend of TOH influenced by NO_2 remains positive, but it varies greatly because of the differences in the signs of anthropogenic emissions. Over oceans, TOH trends are primarily positive in the northern hemisphere, resulting from the upward trends in HCHO, TO_3, and H_2O(v). Using the present framework, we can tap the power of satellites to quickly gain a deeper understanding of simulated TOH trends and biases.

1. Introduction

The hydroxyl radical (OH) regulates the lifetimes of a vast number of key atmospheric compounds, such as sulfur dioxide (SO_2), nitrogen dioxide (NO_2), volatile organic compounds (VOCs), carbon monoxide (CO), and methane (CH_4). Despite its outsized importance for atmospheric chemistry and climate, our knowledge on both the abundance and long-term trends of OH is limited due to its sparse observations, manifesting in large discrepancies between simulated OH among global models (e.g., Naik et al., 2013; Zhao et al., 2019; Murray et al., 2021; Fiore et al., 2024). Particularly, these discrepancies can introduce large uncertainties when it comes to precisely representing methane (Holmes et al., 2013; Nguyen et al., 2020), a potent greenhouse gas. Consequently, to understand the potential impact of this warming agent on climate shifts and extreme weather events, it is essential to accurately simulate methane concentration within a coupled climate model, such as the NASA's Goddard Earth Observing System (GEOS) model (Molod et al., 2015; Nielsen et al., 2017), which requires reasonable representation of its major sink – reaction with OH.

Despite the challenges posed by OH's short lifespan of less than two seconds, low-pressure laser-induced fluorescence spectroscopy has proven invaluable in measuring OH for over twenty airborne field campaigns (Miller and Brune, 2020). These datasets have been instrumental in verifying the efficacy of chemical mechanisms involving varying reaction rate coefficients and aerosol heterogeneous chemistry (Brune et al., 2019; Miller and Brune, 2020; Brune et al., 2022), understanding urban air quality (Brune et al., 2022; Souri et al., 2023), as well as identifying potential sources of HO_x ($OH+HO_2$) that may have been hampered due to instrument detection limits and/or unmeasured compounds (e.g., Ren et al., 2008). However, while these observations offer valuable insights, they are limited in time and space and cannot provide a full picture of tropospheric OH abundance.

There are several approaches that have been employed to constrain OH needed for replicating observed values of a tracer whose primary sink is OH and its sources are relatively well known. One notable method is methyl chloroform (MCF) inversion (Patra et al., 2014; Turner et al., 2017; Rigby et al., 2017;

https://doi.org/10.5194/egusphere-2024-410
Preprint. Discussion started: 29 February 2024

Naus et al., 2019). However, this method only provides hemispheric-average OH and is thus insufficient to resolve the spatial distribution of OH.

A more sophisticated approach to constraining OH is to incorporate well-characterized satellite observations of factors known to influence OH, such as NO_2, CO, ozone, and formaldehyde (HCHO), into a chemical transport model using inverse modeling and/or chemical data assimilation methods (Sandu and Chai, 2011; Bocquet et al., 2015). This method offers a crucial advantage in that it accounts for the interconnectedness of various chemical and physical processes within model increments. For example, adjustments to NO_x levels will impact nitrate and ozone concentrations, which in turn affect the HO_2 uptake through aerosols, OH, and radiation, reciprocally leading to a more accurate representation of NO_x. Several studies have used subsets of satellite observations to improve HO_x and ozone chemistry, with Miyazaki et al. (2020) using a diverse range of observations, including CO, NO_2, O_3, and nitric acid (HNO_3), to improve model predictions using a local ensemble Kalman filter. The incorporation of these observations led to a reduction in the asymmetric OH ratio between the northern and southern hemispheres, aligning better with MCF results (Patra et al., 2014). Similarly, Souri et al. (2020a) leveraged well-characterized observations of HCHO and NO_2 to improve ozone chemistry over East Asia using non-linear analytical Bayesian inversion, observing significant changes in OH levels after adjusting biogenic VOC in southeast Asia. While incorporating these observations into atmospheric models offers a comprehensive way to gain insights into spatiotemporal OH variability, it is complicated by several layers of complexity, such as unidentified satellite biases, unresolved scales in satellite observations, and errors in models including transport, chemical mechanisms, vertical diffusion, and depositions rates. Understanding how these errors could cloud the realistic determination of OH requires running constrained models under various realizations, which is computationally prohibitive.

Researchers have developed OH predictors based on a set of key parameters, offering reasonable spatial and temporal coverage without compromising computational efficiency (Spivakovsky et al., 2000; Duncan et al., 2000; Elshorbany et al., 2016; Nicely et al., 2018; Wolfe et al., 2019; Nicely et al., 2020; Anderson et al., 2022, Zhu et al., 2022; Anderson et al., 2023; Baublitz et al., 2023). These studies fall into four categories, the first of which uses box model photochemical simulations to predict OH levels under a steady-state assumption, using a blend of pre-modeled fields and various observations influencing OH (Spivakovsky et al., 2000; Nicely et al., 2018). The second group uses proxy observations (e.g., HCHO or water, H_2O) of OH in remote areas (Wolfe et al., 2019; Baublitz et al., 2023). The third group employs high-order polynomials to establish an empirical relationship between OH and different parameters, avoiding the need to solve numerous differential equations in chemical mechanisms (Duncan et al., 2000; Elshorbany et al., 2016). Finally, the fourth group leverages powerful machine learning algorithms to encapsulate the complexities between OH and its key influencers to efficiently predict OH using a comprehensive dataset which is easily exchangeable between models (Nicely et al., 2020; Anderson et al., 2022; Zhu et al., 2022; Anderson et al., 2023).

In this work, we demonstrate the potential of a new approach to constrain simulated OH that uses satellite observations to adjust the input parameters to an improved parameterization of OH (Anderson et al., 2022), within the Efficient CH_4-CO-OH (ECCOH) (pronounced "echo") configuration (Elshorbany et al., 2016) of NASA's GEOS model. We use the Modern-Era Retrospective analysis for Research and Applications, Version 2 (MERRA2) reanalysis data (Molod et al., 2015) to constrain meteorology and adjust two critical OH inputs using the latest Aura Ozone Monitoring Instrument (OMI) NO_2 and HCHO retrievals (Lamsal et al., 2021; Nowlan et al., 2023) from 2005-2019 worldwide. Through conducting a range of experiments, we determine the extent to which leveraging OMI NO_2 and HCHO observations can enhance current representations of these two species derived from a global model simulation, MERRA2-GMI (hereafter M2GMI) (Strode et al., 2019), so that we can achieve more accurate portrayals of OH abundance and its long-term trends. Ultimately, we deconvolve the intricate OH trend maps into five critical parameters using various modeling experiments, including tropospheric ozone, stratospheric ozone, NO_2, HCHO, and H_2O.

Our paper is structured into several sections. In sections 2.1 to 2.3, we discuss the model configurations, Bayesian data fusion algorithm, and satellite observations used. In section 2.4, we outline

https://doi.org/10.5194/egusphere-2024-410
Preprint. Discussion started: 29 February 2024

our modeling experiments, which aim to uncover the impact of various key OH inputs on its trends and assess the effect of OMI adjustments. In section 3.1, we examine the discrepancies between our prior knowledge from M2GMI and OMI observations and demonstrate how the data fusion can mitigate these differences. In section 3.2, we delve into the effect of OMI adjustments to NO_2 and HCHO on tropospheric OH (TOH) magnitudes across the globe. In section 3.3, we focus on understanding the long-term effect of a set of key inputs on OH and how well they can replicate our most dynamic representation of TOH. In Section 4, we summarize the potential of using satellite observations in conjunction with well-characterized models to identify biases and long-term trends in TOH and discuss the limitations of our current analysis and potential paths forward.

2. Models, Methods, and Measurements

2.1. Models

2.1.1. GEOS

The GEOS model (Molod et al., 2015; Nielsen et al., 2017) simulates global weather with 1° longitude × 1° latitude spatial resolution. The model follows 72 hybrid sigma values ranging from the surface to 0.01 hPa. We employ a cumulus parameterization to consider deep convection (Moorthi and Suarez, 1992). Cloud microphysics is determined by a single-moment parameterization based on Bacmeister et al. (2006). We activate the "replay" option (Orbe et al., 2017) to constrain several meteorological variables using the MERRA-2. Sea surface temperatures and ice content are pre-described from various observations (Nielsen et al., 2017; Reynolds et al., 2007). Speciated aerosol concentrations and their optical properties are simulated by the GOCART model (Chin et al., 2002) within GEOS. The rapid radiative transfer model for GCMs (RRTMG) resolves the long- and short-wave radiation imposed by GOCART-simulated aerosols, allowing for the direct impact of aerosol on meteorology to be taken into consideration (Nielsen et al., 2017). The period of simulation starts in 2005 and ends in 2020. Ten years before 2005 are considered for the spin-up of meteorological, CO, and CH_4 fields.

2.1.2. ECCOH

A computationally-efficient module, named ECCOH was developed to simulate the chemistry of the CH_4-CO-OH cycle in the GEOS-5 model framework (Elshorbany et al., 2016). CO and CH_4 tracers are explicitly simulated and their emissions are discussed in Sections 2.1.2.1 and 2.1.2.2. A key component of ECCOH is the parameterization of tropospheric OH, which was developed using a gradient boosted regression tree machine learning algorithm (Anderson et al., 2022) and is a function of chemical, solar irradiance, and meteorological variables. The training dataset of chemical and meteorological variables was a 40-year daily M2GMI model simulation (Strode et al. 2019), which includes tropospheric chemistry involving 120 species and 400 reactions with the GMI mechanism (Duncan et al., 2007a and the references therein) and uses MERRA-2 reanalysis to constrain transport and meteorology at 0.625×0.5 degrees.

We present the variables used as inputs to the parameterization of OH for this study in Table 1. The daily archived chemical inputs are from the M2GMI simulation with several variables being constrained with observations. For instance, both NO_2 and HCHO fields are corrected whenever satellite observations are available as described in Section 2.2.1. We chose NO_2, an observable compound from satellites and a reasonable proxy for NO_x that has been shown to affect OH (e.g., Zhao et al., 2020; Anderson et al., 2022). HCHO is used as a proxy for VOC oxidation via OH in remote oceanic regions (Wolfe et al., 2019).

https://doi.org/10.5194/egusphere-2024-410
Preprint. Discussion started: 29 February 2024

There are also long-term satellite data records of other OH drivers, including water vapor (e.g., Aqua AIRS) and total ozone column (e.g., Aura OMI), that we could also consider. However, the GEOS MERRA-2 system already assimilates satellite datasets of water vapor and the M2GMI simulation simulates well (i.e., <4%) the total ozone column as compared to observations (Figure S1). The integrated water vapor columns from MERRA2 and microwave-based satellite observations over-ocean also agree well (<5%), especially after 2000 when many satellite observations have been used in the reanalysis data (Figure 3 in Bosilovich et al., 2017). Therefore, the application of the "replay" mode constrains various meteorological fields, providing a more realistic reconstruction of OH studied here.

Tropospheric ozone is another critical input to the parameterization of OH. Although we will compare M2GMI tropospheric ozone with satellite observations to locate any differences, reliable measurements of tropospheric ozone from satellites are lacking due to the limited sensitivity of the retrievals to ozone in low altitudes. Therefore, our study refrains from imposing any observational constraint on tropospheric ozone.

2.1.2.1. Monthly CO emissions

We use a modified version of EDGAR (Emissions Database for Global Atmospheric Research) v5.0 (Crippa et al., 2019), which is a comprehensive database that provides estimates of sector-based CO emissions from human activities (i.e., anthropogenic) on a global scale. Previous studies (e.g., Zheng et al., 2019) suggested a large underestimation of EDGAR CO emissions for India and China. Accordingly, we scale up the residential and transportation emissions from China by a factor of 1.6, and the residential emissions from India by a factor of 1.2 based on Zheng et al. (2019). The emissions spanned the entirety of the study period, from 2005 until 2020, and were prepared monthly at a spatial resolution of $0.1^{o} \times 0.1^{o}$. The daily biomass burning emissions are CMIP6 emissions, which derived from on the Global Fire Emissions Database version 4 with small fires (GFED4s) (van Marle et al., 2017). To account for the chemical production of CO from the oxidation of non-methane VOCs, we adopt the CO yield estimates from Duncan et al. (2007b) (i.e., a molar yield of 20% from isoprene, 20% from monoterpenes, 100% from methanol, 67% from acetone, 19% from anthropogenic VOC emissions, and 11% from biomass burning VOC sources) and released these CO emissions in the first vertical level of the model. With regards to the biogenic VOC emissions used for the above CO production estimates, we use offline MEGAN calculations using a GEOS-Chem (v13.2.0) run. CO production from CH_4 oxidation is calculated online for each model box.

2.1.2.2. Monthly CH_4 emissions

In this study, several bottom-up CH_4 emissions related to anthropogenic, wetland, natural, and biomass burning sources are used to simulate CH_4. The monthly-basis anthropogenic sources are derived from EDGARv6 (Ferrario et al., 2021). The biomass burning emissions come from the GFED4s. Because EDGARv6 accounts for agricultural waste burning, we exclude this specific source from the GFED4. Following Strode et al. (2020), we use modified monthly-basis natural emissions from ocean, termite, and mud volcano emissions. Wetland emissions are derived from an improved dynamic wetland emission framework at $0.5^{o} \times 0.5^{o}$ based on the TOPography-based hydrological model (TOPMODEL) (Zhang et al., 2016; Zhang et al., 2023). A climatological sink of CH_4 from soil uptake is subtracted from the total CH_4 emissions.

https://doi.org/10.5194/egusphere-2024-410
Preprint. Discussion started: 29 February 2024

Table 1. The list of inputs used for the parametrization of OH.

Input Group	Variables (**Directly Constrained**)	Source	Temporal Resolution
Offline Chemical Species	**NO_2**, **HCHO**, O_3, isoprene, acetone, H_2O_2, propene, propane, methyl hydroperoxide, ethane, C4 and C5 alkanes, and stratospheric O_3 columns	M2GMI (offline) (Strode et al. 2019)	Daily-averaged
Online Chemical Species	CO and CH_4	GEOS (online)	Daily-averaged
Meteorological Fields	**T**, **P**, **Qv**, and cloud fraction	GEOS (online)	Daily-averaged
Optical Properties	Aerosol optical depth; ice crystal cloud optical depth; and water droplet cloud optical depth at above and below of a given model vertical layer.	GEOS (online)	Daily-averaged
Geographic Information	Latitude and solar zenith angle (SZA)	Calculated	Fixed for latitude, but daily for SZA based on local noontime
Surface Properties	Surface UV albedo	OMI LER climatology (Qin et al., 2019; Fasnacht et al., 2019)	Monthly (climatology)

2.2. Methods

2.2.1. Bayesian data fusion for NO_2 and HCHO fields using OMI retrievals

To improve the representation of M2GMI NO_2 and HCHO concentrations and their long-term trends, which are used as input to the parameterization of OH in ECCOH, we scale their columnar mass using Aura OMI observations of NO_2 and HCHO columns (described in Sections 2.3.1 and 2.3.2) using an offline version of the optimal interpolation (OI) method (Parish and Derber, 1992; Jung et al., 2019) with an appropriate regularization. If we assume that the error covariances of M2GMI columns and OMI ones follow a Gaussian distribution with zero means and their relationships are linear, we can estimate new columns using Bayes' theorem (Rodgers, 2000):

$$\mathbf{X}_a = \mathbf{X}_b + \gamma\mathbf{B}\mathbf{H}^{\mathrm{T}}(\gamma\mathbf{H}\mathbf{B}\mathbf{H}^{\mathrm{T}} + \mathbf{E})^{-1}(\mathbf{Y} - \mathbf{H}\mathbf{X}_b) \quad (1)$$

where $\mathbf{X_b}$ is the prior M2GMI columns (i.e., background), $\mathbf{X}_a$ is the posterior M2GMI columns (i.e., analysis), **B** is the error covariance matrix of the a priori, **E** is the error covariance matrix of the observations, **Y** is the observations, and **H** is the observational operator which is equivalent to the identity matrix in our case. **E** is populated by the average sum of precision error squares the satellite product provides. We interpolate both **E** and **Y** into the M2GMI grid box using a mass-conserved linear barycentric interpolation method. The National Meteorological Center's (NMC) approach is a common technique for calculating **B** in atmospheric models (Parish and Derber 1992;

https://doi.org/10.5194/egusphere-2024-410
Preprint. Discussion started: 29 February 2024

Souri et al., 2020b); however, due to computing constraints, rerunning the M2GMI model to create the 24-hour prediction segments needed in the NMC method was not possible. Instead, we initialize **B** by setting it to 50% errors for NO_2 and HCHO, both of which are subject to regularization. γ is the regularization factor designed for achieving the best fit (minimum residuals between **Y** and $\mathbf{HX_b}$) while minimizing the effect of the noise in the observations (minimum variance in $\mathbf{X}_a$). To this end, we seek an optimal regularization factor based on finding the "knee point" in the curve of the incremental regularization factors (ranging from 0.1 to 10) and the degrees of freedom obtained from the optimization. The γ value is determined based on the average of all data points in a month and does not vary from pixel to pixel to ease the interpretation of the result. We did not account for the non-diagonal spatial correlations of **B**, as it requires us to carry out the NMC method. We use the ratio of $\mathbf{X_b}/\mathbf{X_a}$ to uniformly scale the three-dimensional concentrations of the target gas (i.e., NO_2 or HCHO). The error associated with the constrained M2GMI columns can be obtained via

$$\mathbf{S_a} = (\mathbf{I} - \gamma\mathbf{B}\mathbf{H}^\mathbf{T}(\gamma\mathbf{H}\mathbf{B}\mathbf{H}^\mathbf{T} + \mathbf{E})^{-\mathbf{1}}\mathbf{H}) \times \gamma\mathbf{B} \quad (2)$$

The averaging kernels (AK) describe the amount of information gained from the observations are represented by

$$\mathrm{AK} = \mathbf{I} - \frac{\boldsymbol{S_a}}{\mathbf{B}} \quad (3)$$

where **I** is the identity matrix.

In our research, we have created an open-source Python package called OI-SAT-GMI (Souri, 2024), which possesses the ability to download and process OMI level 2 products, perform air mass factor (AMF) recalculation, and conduct mass-conserved interpolation, while also executing the OI algorithm.

In our approach, the adjustments are implemented to the M2GMI output (i.e., a data fusion approach instead of data assimilation one), thereby restricting the full use of improved NO_2 and HCHO representation for more accurate simulation of other chemical compounds impacted by NO_2 and HCHO, including ozone (e.g., Souri et al., 2020a, 2021). Nevertheless, as the accuracy of NO_2 concentrations can significantly impact OH and HCHO is strongly tied to VOC oxidation through OH in remote ocean areas (Wolfe et al., 2019), the adjustments are expected to be beneficial in achieving a more robust representation of OH.

2.2.2. Trend analysis

We determine a linear trend in a time series based on fitting the following equation accounting for a seasonal cycle and shorter frequencies in the observations:

$$\boldsymbol{y} = a_0 + a_1\boldsymbol{t} + \sum_{i=1}^{3} a_{i+1} cos 2\pi\omega_i(\boldsymbol{t} - \varphi_i) \quad (4)$$

The equation comprises several variables, including a_0 as the mean, a_1 as the linear trend, $\boldsymbol{t}$ as time, a_{i+1}, ω_i, and φ_i are the amplitude, frequency, and phase, respectively. We consider three harmonics ($\omega_i = 1,2,3$) to account for seasonal cycle (ω=1) and higher frequencies. To assess the statistical significance of a trend, we employ the Mann-Kendall test and consider a trend to be significant if the linear trend passes the test at a 95% confidence level.

In the context of trend analysis, the careful examination of errors in observations ($\boldsymbol{y}$) is a critical aspect often overlooked. However, when the errors of observations are obtainable, such as those obtained from satellites or constrained M2GMI fields, we determine the parameters by applying a weighted estimation. This estimation is optimized using a Levenberg–Marquardt algorithm. Considering the errors in the observational data deemphasizes more uncertain data, resulting in a more realistic determination of the linear trend.

https://doi.org/10.5194/egusphere-2024-410
Preprint. Discussion started: 29 February 2024

2.2.3. OH response calculations

To elucidate the response of OH to different input parametrizations, such as NO_2, HCHO, and O_3, we determine the semi-normalized sensitivities through a traditional finite difference method:

$$SOH_i = \frac{[OH]_i^{110\%} - [OH]_i^{90\%}}{0.2} \quad (5)$$

where $[OH]_i^{110\%}$ and $[OH]_i^{90\%}$ are OH concentrations from perturbing input parameters (i) by 1.1 and 0.9 scaling factors in the ECCOH offline framework (Anderson et al., 2022).

2.3. Measurements

2.3.1. OMI MINDS tropospheric NO_2 columns

To improve the representation of NO_2 fields used as input to the parameterization of OH, we constrain the archived monthly fields with the most updated NASA standard tropospheric NO_2 product (v4.0; Lamsal et al., 2021) from Aura OMI. Aura has a local equatorial overpass time of 13:45 and nearly daily global coverage. This new OMI product version is improved in multiple aspects as compared to the former products, including surface reflectance and cloud retrieval (Lamsal et al., 2021).

The validation of OMI tropospheric NO_2 columns from the comparison to integrated aircraft spirals obtained from diverse air quality campaigns revealed a good level of correlation (r>0.7) (Choi et al., 2020). However, large mean biases, approximately 40%, were observed. These biases come from various sources, including systematic biases in prognostic data utilized in the retrieval, biases inherent in the aircraft data, spatial representation errors (Judd et al., 2020; Souri et al., 2022), and temporal representation errors. The spatial representation errors have been recognized to notoriously drift the slopes from the unity line in validation studies (Souri et al., 2022). Notably, Choi et al. (2020) achieved a substantial reduction in mean biases, decreasing from 40% to 16%, through the downscaling of OMI data into a finer resolution domain using a regional chemical transport model. Likewise, Pinardi et al. (2020) reduced the biases between MAX-DOAS and OMI NO_2 observations by considering a radial dilution factor to account for the mismatch scales between the satellite footprint and the pointwise observations. These studies showed that the true statistics describing OMI biases are unknown, but they tended to be milder than those derived from directly comparing large pixels with pointwise measurements. It is important to highlight that discrepancies between M2GMI and OMI NO_2 will surpass the reported biases, thereby underscoring the product's reliability over diverse geographical regions.

The long-term trends of tropospheric NO_2 columns have undergone extensive comparative analyses with in-situ observations (Lamsal et al., 2015; Pinardi et al., 2020), regulatory inputs, and assessments of human and biomass burning activities (Duncan et al., 2016; Choi and Souri, 2015a,b; Krotkov et al., 2016; Jin and Holloway, 2015; Souri et al., 2017; Rueter et al., 2014; de Foy et al., 2016; Hickman et al., 2021).

We prefer level 2 over level 3 products to enable the recalculation of AMFs with time-varying shape factors derived from the M2GMI simulation. We removed low-quality pixels using the main quality flag, cloud fraction >30%, terrain reflectivity >20%, and those pixels affected by the "row anomaly" complication. The data product, which has a spatial resolution ranging from ~13 km × 24 km (at nadir) to ~24 km × 160 km (at extremities of the scanline), were then regridded to the M2GMI grid (0.625°×0.5° degrees) using a mass-conserved linear barycentric interpolation method. The AMF recalculation was performed via:

$$VCD_{new} = \frac{VCD_{old} AMF_{old}}{AMF_{new}} \quad (6)$$

https://doi.org/10.5194/egusphere-2024-410
Preprint. Discussion started: 29 February 2024

where VCD_{old} and AMF_{old} are the default states of tropospheric vertical columns and air mass factors. AMF_{new} is determined by summing the product of scattering weights and the M2GMI partial columns from the surface to the tropopause level prescribed in the OMI level 2 data.

2.3.2. OMI SAO total HCHO columns

For the same reason as OMI NO_2, we use OMI SAO total columns based on a newly-developed algorithm framework by Nowlan et al. (2023). The new retrieval represents a major step forward in the surface albedo treatment including the bidirectional reflectance distribution function for land (BRDF) from the MODIS product (MCD43C1 Version 6.1) extended to the UV wavelengths using a principal component algorithm. Since there are no MODIS BRDF data available over water, the algorithm uses the Cox-Munk slope distribution to estimate the surface reflectance of water bodies (Cox and Munk, 1954). An important issue with the long-term record of OMI HCHO measurements is the artificial increasing trend brought on by sensor degradation (Choi and Souri, 2015a,b, Gonzalez Abad et al., 2015). The algorithm uses an earthshine spectrum over the Pacific Ocean with a latitudinal and solar zenith-dependent correction factor described in Nowlan et al. (2023) to mitigate this artifact.

The new SAO algorithm has been validated with Ozone Mapping and Profiler Suite (OMPS) data radiance with respect to Fourier-transform Infrared Spectroscopy (FTIR) in-situ measurements in 2012-2020, showing a relative bias of 30% based on monthly-averaged data (Kwon et al., 2023). While the validation results based on the OMI radiance have not been released yet, it is likely for the biases to stay at roughly the same range of errors at monthly-gridded OMI data onto the M2GMI grid which is comparable to the OMPS footprint (50 km).

Once again, we used Eq.6 to recalculate OMI HCHO total columns with dynamical shape profiles produced during the M2GMI simulation. We remove unwanted pixels using the following criteria: the main quality flag, cloud fraction >40%, and flag for pixels affected by the row anomaly. We then regridded the data to the MERRA-2 GMI grid using the same approach used for OMI NO_2.

2.4. Experiments

We perform a series of experiments to investigate the sensitivity of OH to geophysical variables known to influence or to be tied with OH. Table 2 lists all sensitivity experiments along with their purposes and differences from an analysis (i.e., constrained) experiment. The pillar of all experiments is the analysis experiment (*Sanalysis*) which uses i) chemical variables from a full-chemistry simulation as input to the parameterization of OH in ECCOH (Section 2.1.2; Table 1); ii) transport and metrological fields constrained by MERRA2 reanalysis data (Section 2.1.1); iii) long-term estimates of monthly CO and CH_4 emissions (Section 2.1.2.1 and 2.1.2.2); iv) optical depths of clouds and aerosols along with observed climatology of OMI UV surface albedo; and v) the NO_2 and HCHO fields constrained by the Bayesian data fusion method (Section 2.2.1).

To examine the importance of having NO_2 and HCHO fields constrained with OMI data, we design three experiments imitating *Sanalysis,* but withholding the OI scaling factors one at a time. We then subtract these model outputs from those of *Sanalysis* and name them as *SOMInitro*, *SOMIform*, and *SOMInitroform*.

The other experiments are intended to systematically isolate the chemical effect of a specific driver/proxy of OH trends. Due to the significant impact of NO_2, tropospheric ozone, stratospheric ozone column, and water vapor on the primary or secondary pathways of OH loss/production (Naik et al., 2013; Murray et al., 2013; Strode et al., 2015; Nicely et al., 2018; Zhao et al., 2020; Anderson et al., 2021), we include four experiments (*SOHwv*, *SOHnitro*, *SOHtropozone*, and *SOHstratozone*) to single out each effect on OH trends. Additionally, we include HCHO (*SOHform*), a robust proxy for VOC oxidation via OH in remote ocean regions

https://doi.org/10.5194/egusphere-2024-410
Preprint. Discussion started: 29 February 2024

(Wolfe et al., 2019) to understand how those chemical pathways have changed over time. In these experiments, we set the target driver constant to the monthly values in the first year of simulation, and subsequently subtract these model outputs from *Sanalysis*. Amongst various OH drivers/proxies considered, water vapor exclusively comes from the GEOS online simulation; to isolate the water vapor effect on OH only, we provide fixed water vapor fields from MERRA2 based on the monthly-varying 2005 simulations. Simultaneously, GEOS is allowed to simulate water vapor online to address meteorology.

Using ambient gas concentrations in the ECCOH model poses a challenge in distinguishing the respective factors contributing to their variations. For instance, it is difficult to discern the distinct influences of lightning-produced NO_2 versus anthropogenic NO_2 on the abundance of OH. However, an advantageous feature of our approach is that various observational sources constrain the data fields used via the Bayesian data fusion method or MERRA2 reanalysis data.

Table 2. The experiments designed to assess the effect of various OH drivers/proxies and OMI constraints on TOH trends and magnitudes.

Model Scenario	Term	Difference from the analysis run	Purpose
Analysis (*constrained*)	*Sanalysis*	--	The "best effort" to simulate the evolution of the CH_4-CO-OH cycle from 2005-2019.
Analysis -[a] defaulting to NO_2 M2GMI	*SOMInitro*	Uses archived M2GMI monthly-averaged NO_2 concentration fields.	Isolate the importance of constraining M2GMI NO_2 concentration fields with OMI observations.
Analysis - defaulting to HCHO M2GMI	*SOMIform*	Uses archived M2GMI monthly-averaged HCHO concentration fields.	Isolate the importance of constraining M2GMI HCHO concentration fields with OMI observations.
Analysis - defaulting to NO_2 and HCHO M2GMI	*SOMInitroform*	Uses archived M2GMI monthly-averaged NO_2 and HCHO concentration fields.	Isolate the importance of constraining M2GMI NO_2 and HCHO concentration fields with OMI observations.
Analysis - fixed H_2O vapor	*SOHwv*	The dynamical water vapor fields fed to the parameterization of OH are fixed to the monthly-varying 2005.	Isolate the impact of the long-term trend of water vapor on OH.
Analysis - fixed tropospheric ozone	*SOHtropozone*	M2GMI ozone fields are set to the monthly-varying 2005.	Isolate the impact of the long-term trend of tropospheric ozone burden on OH.
Analysis - fixed NO_2	*SOHnitro*	M2GMI NO_2 fields are set to the monthly-varying 2005.	Isolate the impact of the long-term trend of NO_2 on OH.
Analysis - fixed HCHO	*SOHform*	M2GMI HCHO fields are set to the monthly-varying 2005.	Understand the long-term trend of HCHO strongly tied with VOC oxidation via OH in remote regions.
Analysis - fixed stratospheric ozone column	*SOHstratozone*	M2GMI stratospheric ozone field fed to the parameterization of OH is set to the monthly-varying 2005.	Isolate the impact of the long-term trend of stratospheric ozone columns on OH.

[a] "-" denotes the subtraction operator.

https://doi.org/10.5194/egusphere-2024-410
Preprint. Discussion started: 29 February 2024

3. Results and Discussion

3.1. Spatial distributions and trends analysis of several inputs to the parameterization of OH

We begin our analysis with an examination of the long-term trends and magnitudes of two key inputs (HCHO and NO_2) to the parameterization of OH. Some other key parameters, such as total ozone columns, tropospheric ozone columns, and water vapor are also shown in Figure S1-3, Figure S7-8, and Text S1.

3.1.1. Tropospheric NO_2 columns

We performed two sets of comparisons; the first comparison involves examining the differences in the tropospheric NO_2 columns in the M2GMI relative to those of OMI before and after applying the OI correction. The second comparison focuses on the global 2-D maps of long-term linear trends of OMI, M2GMI prior to and after the Bayesian data fusion correction synched at the satellite viewing condition.

Figure 1 demonstrates the absolute difference in M2GMI tropospheric NO_2 columns with respect to those of OMI before (the a priori) and after (the a posteriori) the data fusion application along with AK in 2005-2019. In-land regions show positive biases over several regions, including central Africa (box A), the Midwest U.S. (box B), and Europe (box C). The same tendency was observed in Anderson et al. (2021). The largest contributor to NO_2 in box A and box C is biomass burning activities (Jaeglé et al., 2005; Giglio et al., 2012), suggesting that either the emission factors and/or the total dry mass burnt were possibly too high in these regions.

M2GMI overestimates NO_2 concentrations in non-urban areas in box B which tend to be more severe during summertime. Although soil NO_x emissions could be the first explanation for this phenomenon, accounting for about 30% of tropospheric NO_2 columns in the region according to Vinken et al. (2014), the soil NO_x parameterization used in M2GMI relies on Yienger and Levy (1995), which is known to have a low bias (Jaeglé et al., 2005; Hudman et al., 2012; Vinken et al., 2014; Souri et al., 2016). Therefore, there may be other uncertainties in the model concerning chemistry (e.g., Canty et al., 2015) or area anthropogenic NO_x emissions (Hassler et al., 2016) causing the bias.

A large portion of metropolitan areas in the Middle East, Europe, and the U.S. shows an underestimation of NO_2 in M2GMI. Moreover, OMI observations reveal large positive biases over the North China Plain (NCP), a region exhibiting exceptionally high NO_2 levels (e.g., Duncan et al., 2016; Krotkov et al., 2016; Souri et al., 2017). This is primarily because of not accounting for the recent aggressive emissions mitigation in China in the bottom-up emission inventory used in the model. We observe several regions over China and Yellow Sea underestimating NO_2 with respect to OMI observations that do not improve considerably after the adjustments. This tendency is a result of the use of a fractional error for populating the error covariance matrix of the a priori, rendering the prior error too low. Although we used a regularization factor to battle this problem, it did not vary from region to region. A regionally-adaptive regularization factor could be a possible remedy for this problem but at a cost of overcomplicating the interpretation of the results.

Expectedly, the Bayesian fusion greatly mitigates the regional biases, with notable reductions observed over central Africa, China, the U.S., Amazon, and Europe. The regional biases (>80%) well exceed the reported biases associated with OMI tropospheric NO_2 product (<40%), suggesting that the adjustments should be considered as improvement. Nonetheless. it is important to acquire an abundance of long-term records from surface spectrometers such as MAX-DOAS and Pandora to comprehensively evaluate the degree of enhancement of M2GMI constrained by OMI within the troposphere, which is currently unavailable for the period of 2005-2019 to our best knowledge. The reduction in the biases over remote areas in the tropics is less noteworthy due to large errors in the observations. In other words, it is difficult to have high confidence in the degree of deficiency the model can have in simulating NO_2 over pristine areas by comparing it to OMI. This notion mathematically manifests in low AK in remote areas showing that rich information from OMI tropospheric NO_2 gravitates more towards polluted regions.

https://doi.org/10.5194/egusphere-2024-410
Preprint. Discussion started: 29 February 2024

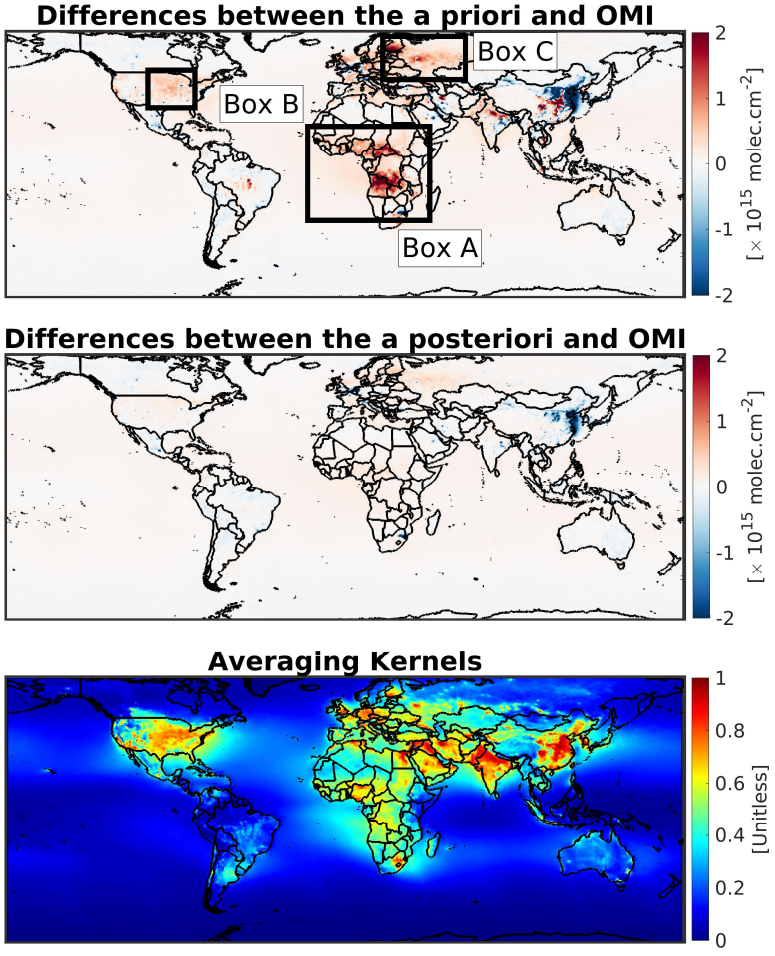

Figure 1. The global maps of M2GMI tropospheric NO_2 annual difference with respect to those of OMI before applying the Bayesian data fusion correction factors (top) and after (middle) in 2005-2019; the mean of averaging kernels describing the gained information from OMI (bottom). Grids in high latitudes are removed from the figure due to too few numbers of samples OMI provided.

Figure 2 illustrates the linear trends of tropospheric NO_2 between 2005 and 2019 observed by OMI and simulated by the M2GMI before and after using the OI algorithm. The errors in OMI observations and the constrained M2GMI are considered while calculating the trends. Focusing on the trends by OMI, we observe a consistent picture compared to former studies (Duncan et al., 2016; Choi and Souri, 2015a,b; Krotkov et al., 2016; Jin and Holloway, 2015; Souri et al., 2017). High income countries, such as the U.S., those located in the western Europe, and major cities in Russia, undergo a significant reduction of NO_2 concentrations due to the implementation of emission mitigation regulations. Additionally, low and moderate income countries, such as those in the Middle East, northern Africa, and India, have seen upward trends in NO_2. Various signs of trends are observed in East Asia. Due to recent effective regulations in China (Zhang et al., 2012), we observe downward trends in the NCP region (Rueter et al., 2014; de Foy et al., 2016; Souri et al., 2017). The downward trend predominantly starting from 2011-2012 counteracts the upward trend in prior years resulting in

https://doi.org/10.5194/egusphere-2024-410
Preprint. Discussion started: 29 February 2024

statistically insignificant linear trends. Both Japan and South Korea show downward trends during the period of 2005-2019 (Duncan et al., 2016; Souri et al., 2017).

Encouragingly, the model prior simulation of the tropospheric NO_2 trend is consistent with OMI over most of the polluted regions except for China, where the bottom-emission inventories used in the M2GMI fail to reflect recent mitigation efforts occurring in NCP region. The posterior estimation is in a higher degree of agreement compared to OMI (Text S2). An encouraging observation arising from the comparison of the M2GMI prior with the posterior NO_2 trends is the achievement of a higher spatial variance (information) in low and medium income countries (e.g., India and Iran). This finding suggests that the emission inventories used in the M2GMI lacked adequate spatial information even at the model spatial resolution.

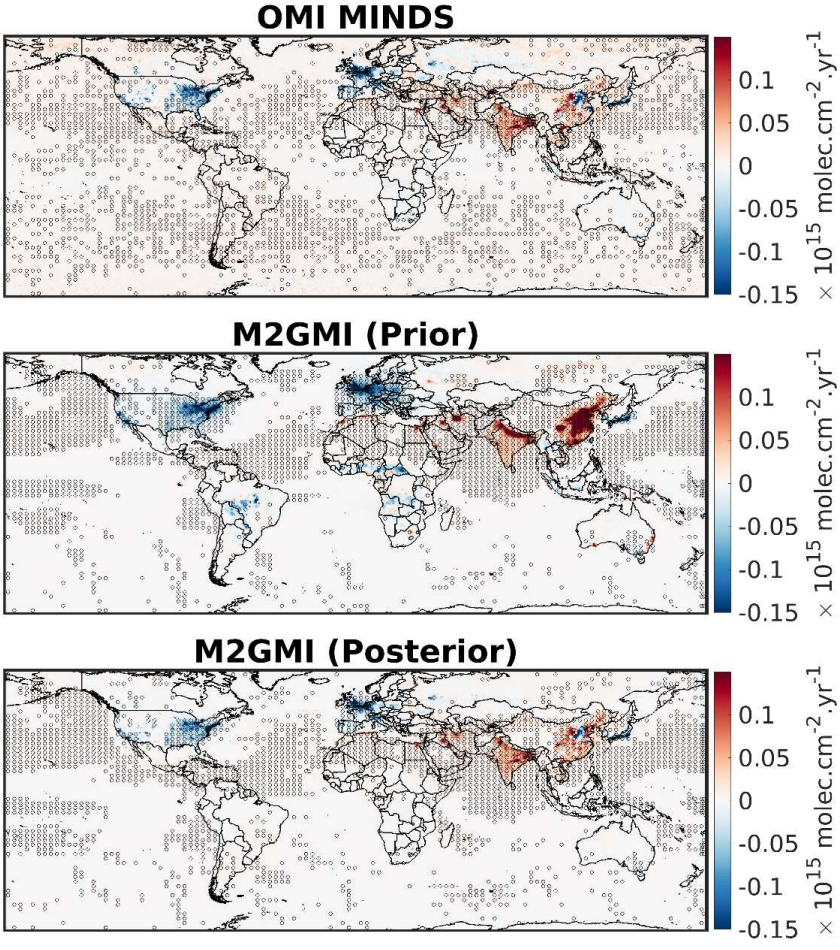

Figure 2. The global maps of linear trends of annual tropospheric NO_2 columns observed by OMI and simulated by M2GMI before and after using the Bayesian fusion. The model simulations are sampled at the exact time and location of OMI, and masked if OMI observations were unavailable due to data quality criteria used. The dots indicate statistically significant trends at 95% confidence interval.

https://doi.org/10.5194/egusphere-2024-410
Preprint. Discussion started: 29 February 2024

3.1.2. Total HCHO columns

We validate the simulated HCHO concentrations, drawing inspiration from the NO_2 comparison framework. Figure 3 illustrates the absolute differences in simulated HCHO total columns with respect to OMI before and after the Bayesian data fusion application, in addition to AK. The prior model simulation has considerable skill in capturing the HCHO total columns over several areas, such as the Middle East, Europe, India, and East Asia. However, marked positive biases are discernible in regions with abundant isoprene emissions, such as the Amazon, southeast Asia, southeast U.S., and central Africa. This outcome is most likely due to an overestimation of biogenic emissions; various investigations have reported a predominantly positive bias (between a factor of 2 to 3) linked to isoprene emissions estimated by the Model of Emissions of Gases and Aerosols from Nature (MEGAN) using satellite measurements in isoprene-rich regions (e.g., Millet et al., 2008; Stavrakou et al., 2009; Marais et al., 2012; Bauwens et al., 2016; Souri et al., 2020a).

The simulated HCHO concentrations are relatively too low over pristine areas, such as high latitudes and over mountains. This may be attributed to an underestimation of CH_4 in M2GMI because of assigning its values as background conditions (Strode et al. 2019). The integration of OMI satellite data has proven effective at reducing the biases in areas where HCHO concentrations are large because the signal-to-noise ratio tends to be large resulting in high AKs. Nonetheless, there are some adjustments over remote areas. In fact, OMI HCHO columns provide more information than OMI NO_2 in remote areas because background HCHO concentrations are not extremely low due to evenly distributed methane and methanol concentrations. It is worth noting that the biases in M2GMI well exceed the expected OMI HCHO column biases, suggesting that the adjustments to HCHO improve the model.

https://doi.org/10.5194/egusphere-2024-410
Preprint. Discussion started: 29 February 2024

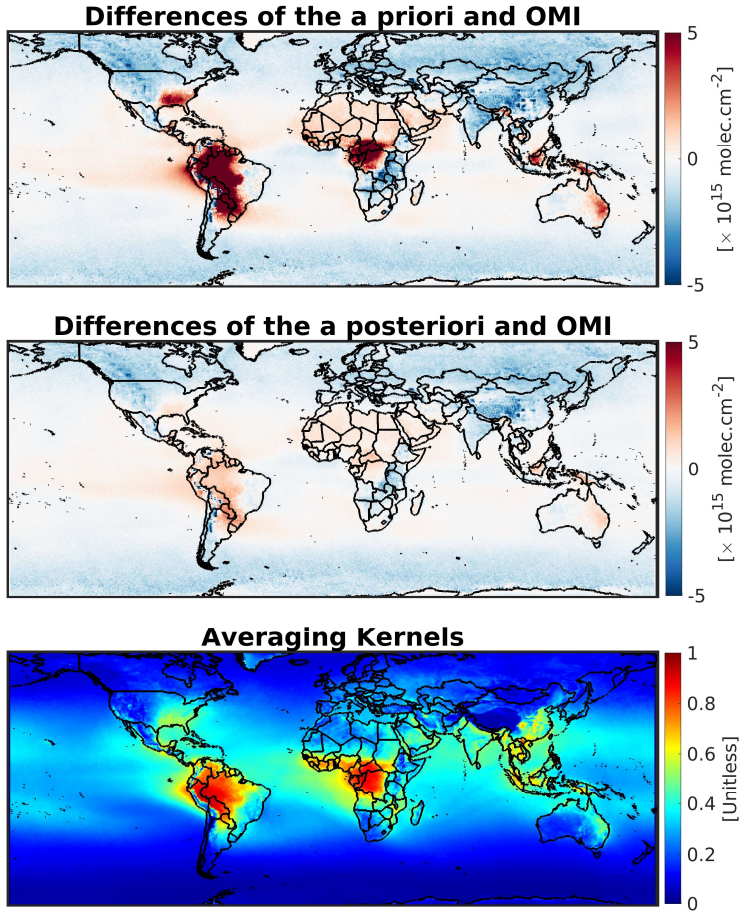

Figure 3. Same as Figure 1 but for HCHO total columns.

Figure 4 shows the global maps of HCHO total column trends derived from OMI, the prior M2GMI, and the posterior M2GMI. The widespread upward trends in HCHO over India are evident due to lack of effective efforts on cutting emissions related to volatile organic compounds (e.g., De Smedt et al., 2015; Kuttippurath et al., 2022; Bauwens et al., 2022). We observe HCHO columns going up in the northwestern US and over oil sands in Canada, possibly due to increased evergreen needleleaf forest and an increase in crude oil production (Zhu et al., 2017), respectively. The downward trends over the southeast US could be due to a decrease in drought events (Figure S5), which significantly affect isoprene emissions and the oxidation of VOCs (Duncan et al. 2009; Naimark et al., 2021; Wang et al., 2022). Alternatively, this downward trend could be partially due to the dampened HCHO production from VOC oxidation due to reduced NO_x emissions (Marais et al., 2014; Wolfe et al., 2016; Souri et al., 2020c). In agreement with previous studies (Stavrakou et al. 2017, Souri et al., 2017, Shen et al., 2019, Souri et al., 2020a), HCHO columns increase over the NCP. HCHO columns tend to decrease over parts of central Africa (e.g., Democratic Republic of the Congo) and the Amazon basin potentially due to reduced deforestation rates (De Smedt et al., 2015; Jones et al., 2022). However, a large variability in the sign of HCHO trends over these regions is seen; Congo shows an opposite trend in comparison to that of Democratic Republic of the Congo; the northern portion of the Amazon basin increased. Encouragingly, the prior knowledge captures the upward trends over India and China along with

https://doi.org/10.5194/egusphere-2024-410
Preprint. Discussion started: 29 February 2024

downward trends over central Africa. However, the magnitudes and spatial features of these trends are not entirely in line with respect to OMI.

We do not fully understand HCHO trends over oceans. Part of these patterns might be caused by transport from nearby sources. For instance, areas around south Asia, South America, and Gulf of Mexico are affected by the trends over the land in their proximity. However, trends over several areas, such as the southern part of the Indian Ocean, Australia, and Sahara, are not fully explainable by nearby sources. It is possible that certain patterns can be linked to climate variability; for instance, there is growing evidence of more cyclonic circulation intensifying westerly trade winds from central Africa due to warming Indian Ocean (Dhame et al., 2020) that may contribute to rising HCHO. An in-depth understanding of HCHO trends over oceans certainly deserves a separate follow-up study.

The posterior estimates better line up with the OMI trends, especially over the Amazon, India, and Central Africa (Text S3). The correction factors, however, worsen the trends over the southeast US and Canada. This is essentially due to the use of the fractional errors in the a priori making the OMI corrections more impactful (i.e., higher Kalman gain) in summertime than in wintertime.

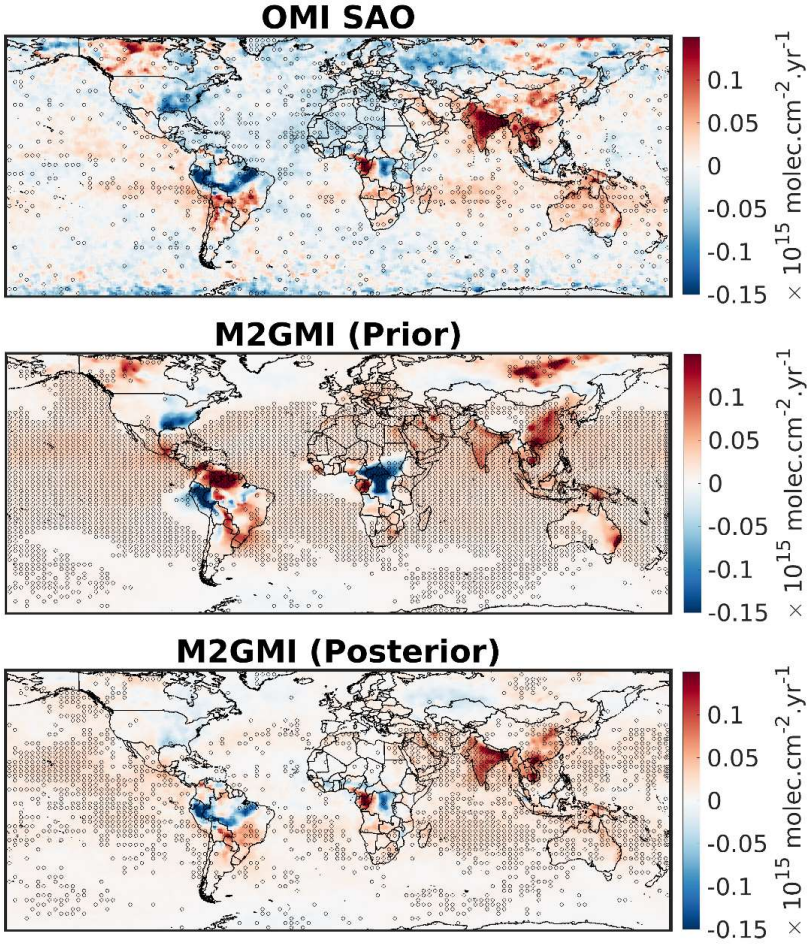

Figure 4. Same as Figure 2 but for total HCHO columns. The linear trends in OMI SAO are smoothed by a median filter for better visualization.

https://doi.org/10.5194/egusphere-2024-410
Preprint. Discussion started: 29 February 2024

In sum, we saw that M2GMI NO_2 and HCHO, both inputs to the parameterization of OH, were broadly better presented through the integration of OMI observations. Consequently, the improvement is expected to elevate the level of reliability in the experimental outcomes, particular in the context of *SOHnitro* and *SOHform* simulations. As for other important compounds, such as stratospheric columns, tropospheric O_3, and water vapor, the comparison of the model with OMI total ozone columns shows a strong degree of agreement (<4% biases) with no significant trend in low-mid latitudes (Figure S1 and S2). The well-documented upward trend in tropospheric ozone in the northern hemisphere is well reproduced by M2GMI (Figure S3). We did not validate GEOS water vapor simulations, because of the use of MERRA2 reanalysis, which is thoroughly validated in Bosilovich et al. (2017). Furthermore, the comparison of integrated water vapor linear trends from our GEOS-5 run (2005-2019) with satellite data presented in Borger et al. (2022) shows a remarkable agreement (Figure S7-8).

3.2. Added value of OMI on simulated tropospheric OH

Here, we present the results from three OMI-related experiments (*SOMInitro*, *SOMIform*, *SOMInitroform*) to understand the effect of OMI adjustments made to M2GMI on TOH. Throughout the paper, TOH is determined based on the methane-reaction-weighted OH suggested by Lawrence et al. (2001). Moreover, we calculate the response of TOH to NO_2 and HCHO using Eq.5.

Figure 5 consists of three columns, illustrating the percentage adjustments made by OMI NO_2 using OI, the response of TOH to NO_2 concentrations, and the simulated TOH derived from the *SOMInitro* experiment. The observed pattern of increments aligns with the improvements seen in Figure 1, with positive (negative) values indicating underestimation (overestimation) of M2GMI. Broadly, the overestimates dominate over underestimates resulting in the global tropospheric NO_2 reduction by ~4%. Upon segregating the increments into four distinct seasons, it becomes evident that the adjustments do not uniformly apply to every season. This non-uniformity is primarily attributed to biases in M2GMI, influenced by biomass burning (box A, C) (Section 3.1.1), both of which exhibit strong seasonality.

Deciphering the precise chemical processes influencing the response of OH to NO_2 using a machine-learning approach is challenging. However, it is widely recognized that NO_x has positive feedback on OH through increased $NO+HO_2$ and ozone (Murray et al., 2021; Zhao et al., 2020; He et al., 2021). Considering NO_2 as a surrogate for NO_x, similar tendencies are expected, as evident from the positive numbers from the sensitivity results obtained from offline calculations. The response of TOH to NO_2 displays a pronounced seasonal cycle stemming mainly from photochemistry.

The impact of adjustments made by OMI NO_2 on TOH is most substantial over regions where both the adjustments and TOH responses to NO_2 are significant. For instance, the large adjustments made over Europe in DJF do not substantially affect TOH because the response value is low due to reduced photochemistry.

On a global scale, changes to TOH are much milder (1% reduction) than those occurring regionally. For instance, we see substantial regional impacts (up to 20%) over many areas such as Central Africa, the Midwest US, the Middle East, and Eastern Europe. In light of the global reduction in OH, we observe global column average methane mixing ratios (XCH_4) to increase by 10 ppbv on average (Text S4). This augmentation happens monotonically with an increase of 0.9 ppbv per year, ultimately resulting in ~15 ppbv difference at the end of the simulation (Figure S13). This is essentially due to the long lifetime of CH_4. Likewise, the TOH reduction results in column average CO mixing ratio (XCO) enhancements which transpire more locally than XCH_4 does due to the shorter XCO lifetime. The XCO enhancements reach above 10 ppbv in Africa (Text S5).

https://doi.org/10.5194/egusphere-2024-410
Preprint. Discussion started: 29 February 2024

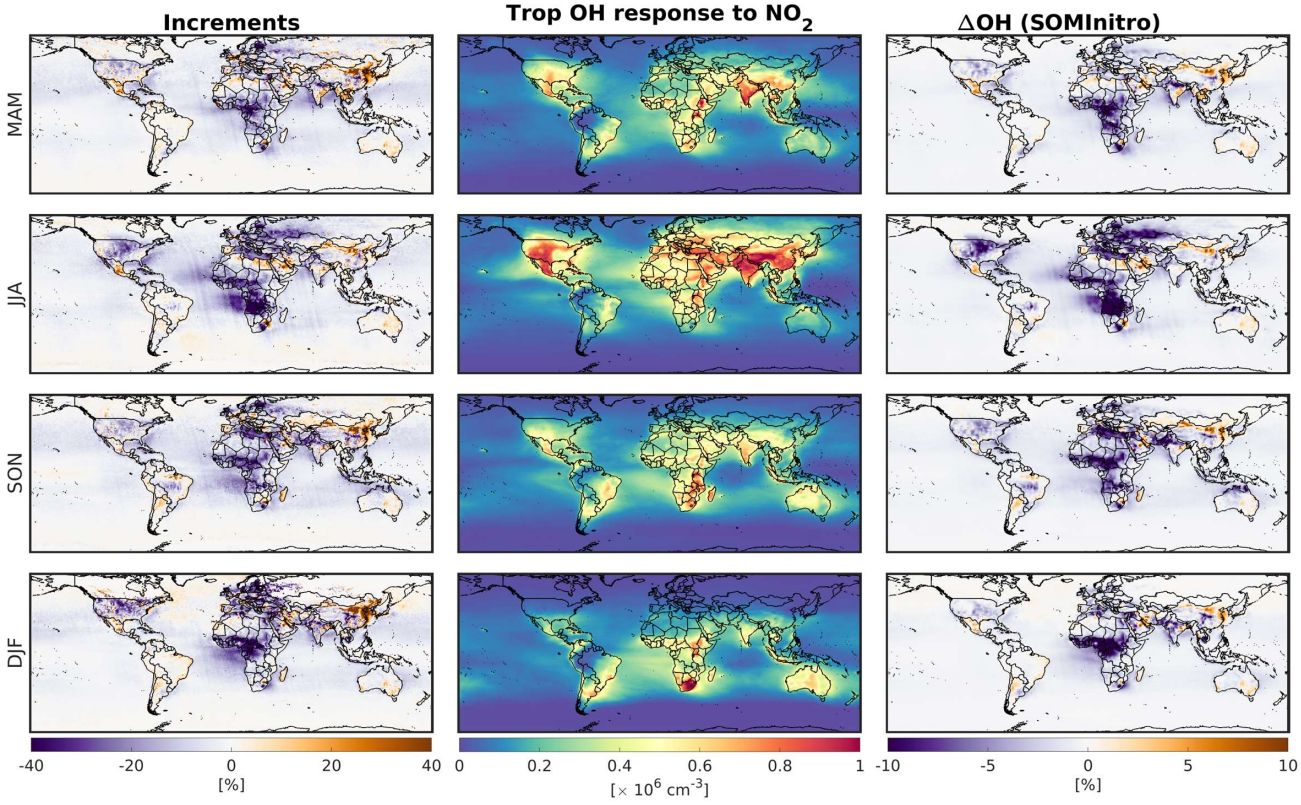

Figure 5. (first column) the percentage of adjustments applied to M2GMI NO_2 fields within the troposphere suggested by OMI tropospheric NO_2 columns for four different seasons, (second column) the semi-normalized response of tropospheric OH to tropospheric NO_2 changes based on ECCOH offline calculations, and (third column) the resulting effect of the adjustments on tropospheric OH derived from the online simulation (*SOMInitro*). MAM, JJA, SON, and DJF are acronyms for March-April-May, June-July-August, September-October-November, and December-January-February.

Figure 6 demonstrates the same scheme as Figure 5 but with a focus on the *SOMIform*. Marked negative increments are found in regions characterized by elevated isoprene concentrations because of the overestimations of M2GMI biogenic isoprene emissions. Positive increments are mostly confined to high latitudes and certain areas of East Asia (Section 3.1.2).

The interplay between HCHO and OH is contingent on the intricate dynamics governing HCHO production from the oxidation of VOCs and methane and HCHO loss from various chemical pathways (Valin et al., 2016; Wolfe et al., 2019). In remote areas where HO_x is low, the prevailing sink of HCHO is through photolysis. Conversely, in more polluted areas, the reaction of HCHO+OH emerges as a competing loss pathway. Assuming a steady-state approximation, which is a reasonable assumption for pristine areas, the photolysis loss of HCHO dominates over the reaction with OH, resulting in a linear relationship between HCHO and OH. In other words, high (low) HCHO concentrations are indicative of high (low) TOH. It is because of this that we use HCHO as a proxy of TOH in remote oceans regions. In regions characterized by heightened HO_x levels, OH and HCHO become decoupled. Encouragingly, our implicit parametrization of OH has considerable skill at elucidating these intricate chemical tendencies; specifically, it reveals muted

https://doi.org/10.5194/egusphere-2024-410
Preprint. Discussion started: 29 February 2024

responses in regions with relatively tangible pollution levels, whereas positive responses are evident in oceanic regions. Like results obtained for NO_2, the response map has a seasonal cycle due to photochemistry.

Because of the muted response of TOH to HCHO over land, a substantial portion of geographical regions undergoing significant adjustments made by OMI becomes less important. TOH primarily changes over oceanic areas in a way that it decreases in low latitudes but increases in high latitudes. The largest reduction occurs in Amazon downwind where both increments and responses display large magnitudes. As a result of these changes, we see a marginal increase in XCH_4 over tropics where OMI increments reduced TOH. The HCHO adjustment did not noticeably affect XCO either (Text S5).

Modifications on HCHO by OMI do not signal substantial changes in background VOC oxidation through OH. In fact, TOH changes by this proxy are of an order of magnitude less than those by OMI NO_2. This tendency is a result of two key factors: i) the adjustments wield their major influence over oceans where M2GMI has a fair performance, and ii) the amount of information obtained from OMI HCHO (i.e., AK) remains somewhat limited in remote areas due to low signal-to-noise ratios.

Due to the rather independent nature of the TOH responses to NO_2 and HCHO, where the former prevails over land and the latter over ocean, the concurrent adjustments of HCHO and NO_2 using OMI (i.e., *SOMInitroform*) results in a rather linear combination of outcomes derived from *SOMIform* and *SOMInitro* (Figure S21). This linear outcome is characterized by a large decrease in TOH in low latitudes and a moderate increase in high latitudes resulting in a decrease of global TOH by ~1%.

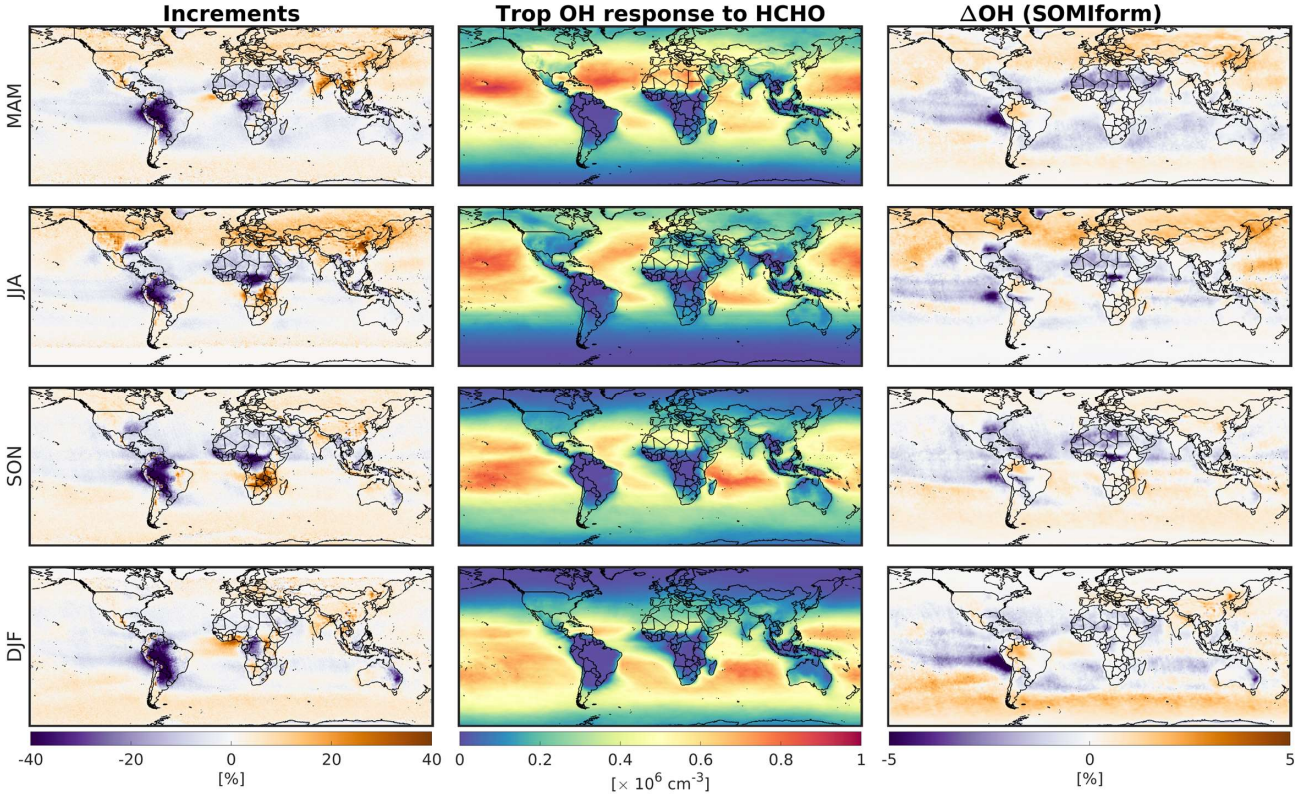

Figure 6. Same as Figure 5 but for HCHO.

https://doi.org/10.5194/egusphere-2024-410
Preprint. Discussion started: 29 February 2024

3.3. Synergy of the model and satellite observations to explain TOH long-term trends

3.3.1. The dominant contributor to TOH trends

Here, we take advantage of the wealth of information from satellites and our well-characterized model used for the inputs to the parameterization of OH to rank the dominant contributor to TOH linear trends. By assuming that TOH follows a linear combination of each individual experiment designed to isolate OH driver/proxy (i.e., *SOHnitro*, *SOHform*, *SOHtropozone*, *SOHstratozone*, and *SOHwv*), wherein second (or higher) chemical feedback is disregarded, we can determine the biggest contributor to the TOH trend for each model grid box by finding which driver/proxy holds the largest absolute amount. We only label a grid if the absolute linear trend of the dominant driver/proxy surpasses the second most dominant one by 30%.

Figure 7 illustrates the dominant factor explaining TOH trends. Several patterns can be found from this result: i) NO_2 plays a significant role in TOH trends in various polluted areas, such as Asia and the Middle East; ii) the upward trend of TOH over the western Pacific Ocean is primarily attributed to increased tropospheric ozone from Asia (e.g., Lin et al., 2017); also, we observe a significant fraction of TOH over the tropical Atlantic Ocean increasing because of rising tropospheric ozone from Africa and Central/South America (Edwards et al., 2003); iii) HCHO is convolved with TOH trends over tropical oceans); iv) water vapor plays a pivotal role in shaping TOH trends over oceans across the globe; iv) stratospheric ozone columns are mostly significant over the South Pole due to the ozone healing process (Figure S2). The next sections will focus on the magnitude of these trends and the degree to which they can collectively explain the variance in TOH trends compared to *Sanalysis*.

It is important to recognize that the analysis presented here should be interpreted as a relative assessment of a limited number of TOH drivers/proxies, rather than an exhaustive evaluation of all the physical and chemical processes that are tied to TOH. Nonetheless, the data presented offers valuable insights into the TOH trends and can be used as a basis for further research.

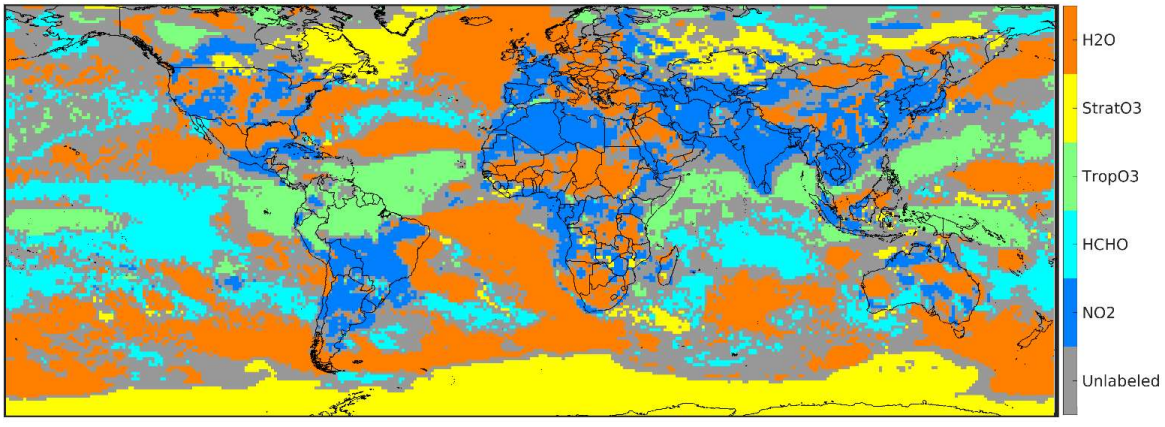

Figure 7. The major contributor to TOH trends based on the largest absolute trends of TOH drivers/proxies above 30% of the second most dominant factor.

3.3.2. Magnitudes of linear trends of TOH key inputs

Figure 8 shows the linear TOH trends influenced by NO_2 (*SOHnitro*), HCHO (*SOHform*), water vapor (*SOHwv*), tropospheric ozone (*SOHtropozone*), and stratospheric ozone (*SOHstratozone*). A discussion on each parameter will follow:

https://doi.org/10.5194/egusphere-2024-410
Preprint. Discussion started: 29 February 2024

SOHnitro – The trends in TOH driven by NO_2 show a strong correlation with the a posteriori trend discussed in Section 3.1.1, with low- and medium-income countries experiencing an increase in TOH due to rising NO_2 levels, while high-income countries see a reduction in TOH due to the opposite trend. The most significant increase in TOH is observed over India, where both the NO_2 trend and TOH sensitivity to NO_2 are prominent. The most rapid regional decline in TOH seems to be over the NCP, because of NO_x reductions that began after 2011. This finding is particularly noteworthy since M2GMI did not reproduce this trend without OMI as a constraint. The trend in TOH resulting from NO_2 is predominantly anthropogenic in nature. This aligns with the findings of Chua et al. (2023), who observed that the impact of lightning NO_x emissions on TOH trends was relatively minor. The global trend in TOH driven by NO_2 is positive, but with considerable variation due to the significant disparities in how anthropogenic NO_x emissions have changed.

SOHform – We saw that HCHO was a reasonable proxy for TOH over oceans. Accordingly, the TOH trends primarily are observed over oceans, especially over the Pacific and the Indian Oceans. This lines up with the information gathered from the analysis of M2GMI and OMI HCHO observations (Figure 4). These upward HCHO trends, as discussed in Section 3.1.2, may be influenced by transport and dynamics. It is worth noting that the increase in TOH tied to this proxy (HCHO) is a global tendency, attributable to the relatively uniform rise in HCHO levels across oceans.

SOHwv –Water vapor is a primary source of OH. The offline sensitivity of ECCOH captures this tendency (Figure S22). Accordingly, the TOH linear trends mirror those of IWV (Figure S8) with major increases over oceans. Similar to other experiments, the global TOH increases because of rising water vapor in the atmosphere. We acknowledge that understanding the reasons for changes in water vapor, which our model shows to agree with Broger et al. (2022), is a complex subject that goes beyond the scope of our research. It requires an in-depth understanding of the water cycle, evapotranspiration and precipitation rates, and the effect of temperature on the air's capacity to hold moisture, known as the Clausius Clapeyron relationship. However, a great deal of effort has been made to demonstrate that global water vapor levels have increased significantly in recent decades. This is based on reanalysis data, microwave satellites, and in-situ measurements (Trenberth et al., 2005; Chen and Liu, 2016; Wang and Liu, 2020; Allan et al., 2023), which is consistent with what our model shows, as it is well-constrained by MERRA2 reanalysis data.

SOHtropozone – The impact of tropospheric ozone on OH formation is widely acknowledged (Lelieveld et al., 2016). Likewise, our ECCOH offline sensitivity tests have revealed a largely positive correlation between tropospheric ozone and OH (Figure S23). Consequently, the linear trends observed in TOH closely mirror those of tropospheric ozone in M2GMI (Figure S3). This tendency is especially noticeable in the Atlantic Ocean, East and Southeast Asia, as well as the northern region of the Pacific Ocean, where rising ozone levels have increased TOH. M2GMI suggests that tropospheric ozone levels in the southern hemisphere have decreased, potentially leading to a downward trend in TOH, an observation that has yet to be fully confirmed (e.g., Thompson et al., 2021). This finding is especially important given past research indicating that models tend to exaggerate TOH asymmetry between the northern-southern hemispheres (Strode et al., 2015; Naik et al., 2013). The decrease in the simulated tropospheric ozone may offer a plausible explanation for this tendency, but further verification is deemed necessary. Like the previous experiments, tropospheric ozone on average leads to a global increase in TOH in 2005-2019.

SOHstratozone –Stratospheric ozone columns reduce UV actinic fluxes leading to a reduction in tropospheric JO^1D and thus OH, a tendency well reproduced by ECCOH (Figure S24). Nonetheless, stratospheric columns did not change noticeably in the tropics and mid-latitudes where OH production is important; consequently, the linear trends are close to zero or faintly negative due to a slight upward trend in the column. This tendency results in a rather uniform decrease of TOH globally.

https://doi.org/10.5194/egusphere-2024-410
Preprint. Discussion started: 29 February 2024

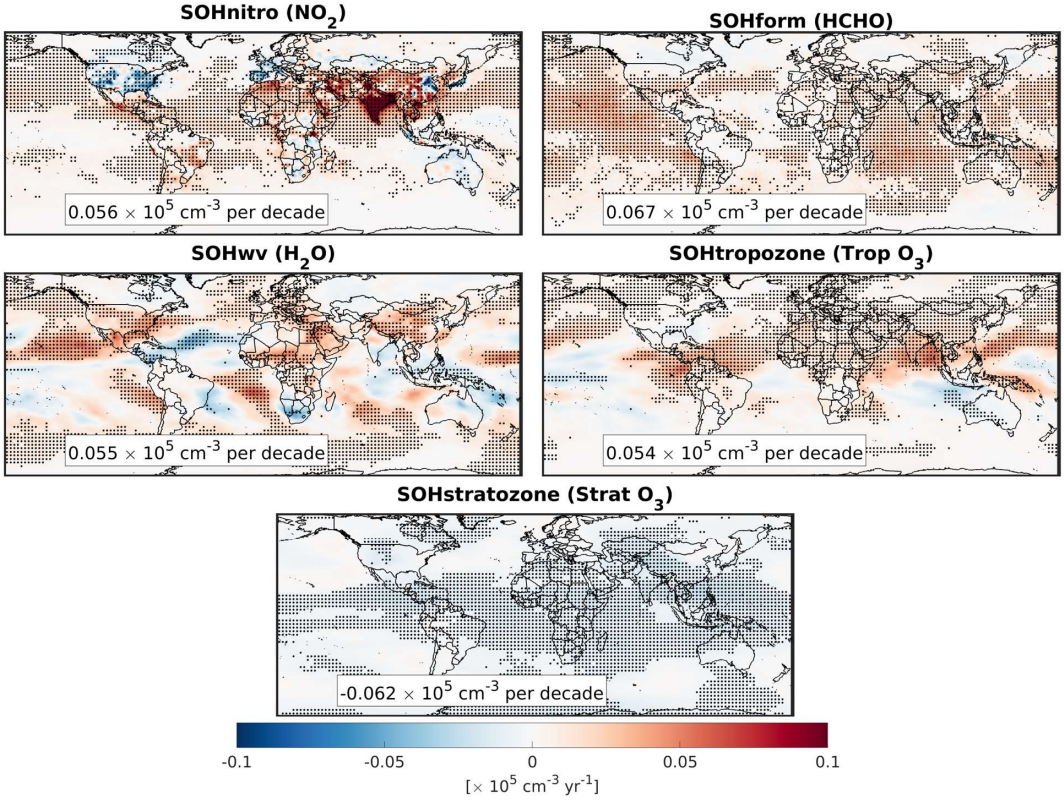

Figure 8. The contribution of each TOH key input (addressed in this study) to TOH in 2005-2019. HCHO, NO_2, and water vapor results are observationally constrained. Stratospheric ozone columns yielded comparable results compared to total ozone columns observed by OMI, however a large portion of tropospheric ozone trend has remained unverified in the southern hemisphere. ENSO affects the variability of TOH (Anderson et al., 2021), so we add a linear term to Eq.4 that is a function of the Niño 3.4 Index. This helps prevent ENSO from affecting the subsequent results.

3.3.3. OMI contributions to TOH trends

It is attractive to gauge the additional information gained from OMI on better representing the linear trends of TOH. To achieve this, we need to analyze three sets of model output: one with OMI scaling factors, one without OMI scaling factors, and one with the NO_2 and HCHO drivers (i.e., *SOHnitro* and *SOHform*). The linear trends from these sets of model results are shown in Figure 9. The trends in the first column illustrate the overall effect of NO_2 and HCHO on TOH trends, while the two other subplots isolate the effect of OMI from the prior information based on M2GMI. It is immediately apparent that the trends in the driver can be well approximated as the linear combination of the other two experiments, suggesting that the second (or higher) order chemical feedback does not heavily affect the results. M2GMI plays a significant role in shaping the trends in *SOHnitro*, possibly due to the small discrepancy between the trends in OMI and M2GMI columns over regions where TOH is responsive to the driver. The most significant impact of OMI on NO_2 is visible over NCP. Concerning HCHO, OMI slows down the upward trends in TOH over oceans which was suggested by M2GMI. In general, M2GMI largely dictates the overall shape of TOH trends driven by NO_2 and HCHO possibly due to small difference between the model and OMI observations and/or limited informational content in OMI.

https://doi.org/10.5194/egusphere-2024-410
Preprint. Discussion started: 29 February 2024

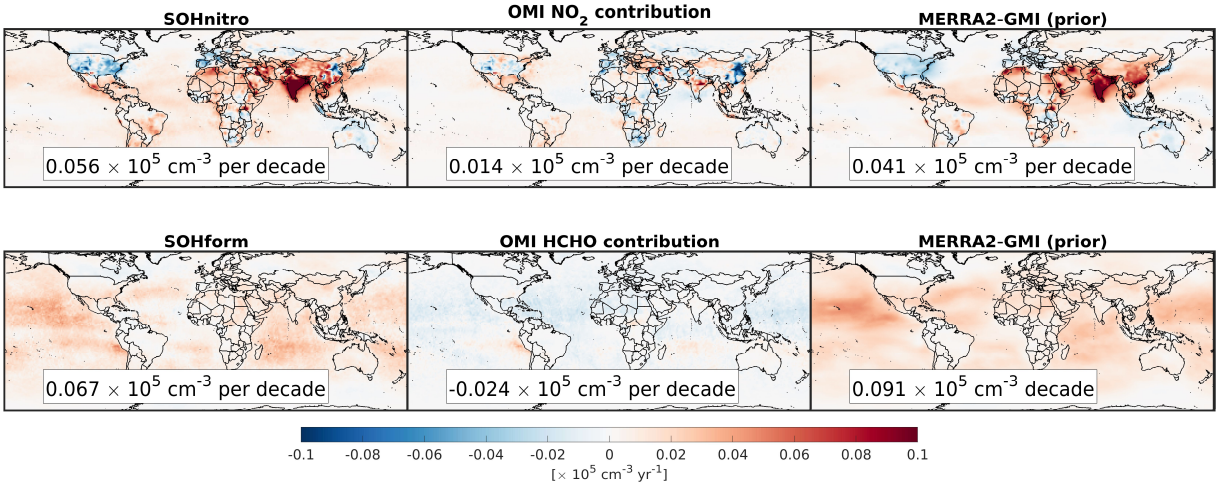

Figure 9. The resulting effect of tropospheric NO_2 and HCHO on TOH linear trends during 2005-2019 (first column); the contributions of OMI information added on top of the prior knowledge (M2GMI) (middle column); the effect of the prior knowledge on shaping TOH linear trends (last column).

3.3.4. How well can these experiments explain the simulated trends collectively?

We find that there is a good degree of correlation between the sum of the linear trends and those of *Sanalysis* (R^2=0.65) indicating that a good portion of variability in TOH trend can be well explained by these experiments (Figure S25). Figure 10a shows the linear trend of TOH from *Sanalysis* in 2005-2019, and Figure 10b shows the sum of the linear trends of the five OH key inputs. These maps are one of the most recent and detailed TOH trends available, relative to newer studies (Nicely et al., 2018; Zhao et al., 2020; Chua et al., 2023). The TOH trend from *Sanalysis* varies greatly, where positive values are prevalent over northern parts of the Pacific Ocean, the Middle East, central Africa, and several regions over East Asia. Negative trends are found over the US, southeast Asia, and the southern part of the Pacific Ocean. The linear sum of the experiments strongly aligns with *Sanalysis*, particularly over the northern hemisphere, reinforcing that the selected parameters are sensible choices to reproduce a large portion of variance in TOH trend.

https://doi.org/10.5194/egusphere-2024-410
Preprint. Discussion started: 29 February 2024

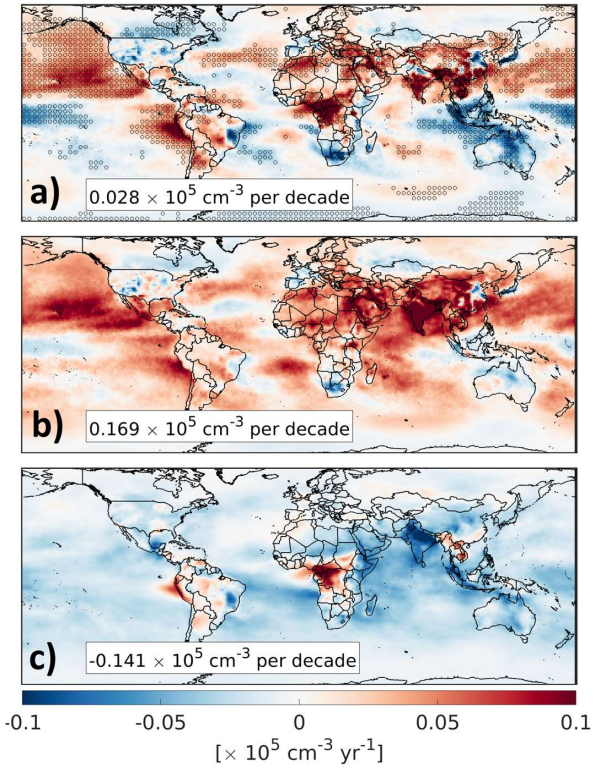

Figure 10. (a) The linear trends derived from *Sanalysis* experiment, the "best effort" to simulate the evolution of the CH_4-CO-OH cycle, from 2005-2019. The statistically significant trends are superimposed by dots. (b) The linear summation of the five selected TOH influencers including water vapor, NO_2, HCHO, stratospheric and tropospheric ozone, showing a strong degree of correspondence to the top panel, particularly in the northern hemisphere. (c) The unexplained portion of the TOH trends, which was not explainable by five experiments addressed in this research.

Revealing the unexplained portion of TOH trends, which cannot be attributed to the selected TOH experiments, is necessary. Within the model, various physiochemical factors such as CO, CH_4, dynamics, aerosols, and clouds can impact the TOH trends. Although we will not delve into these drivers in this study, we can identify unexplained parts of TOH trends by subtracting the sum of trends derived from the five primary TOH key inputs from those of *Sanalysis*, which discounts second (or higher) chemical feedback. Figure 10c displays the unexplained TOH trends between 2005 and 2019. It is readily apparent that there are uniform and significant downward trends in TOH in the tropics and subtropics where photochemistry is strong. This is most likely triggered by increasing concentrations of CH_4, which is demonstrated in Figure S10, causing OH levels to decrease over time. It is very probable that the extent of these downward trends in TOH has been exaggerated in our model because of the simulated CH_4 increasing too rapidly compared to in-situ observations. Consequently, the globally-averaged TOH trend derived from *Sanalysis* may be slower than it should be. Lastly, an unexplained strong upward trend in TOH over central Africa lingers.

https://doi.org/10.5194/egusphere-2024-410
Preprint. Discussion started: 29 February 2024

4. Conclusion

While a comprehensive multi-sensor/multi-species data assimilation and inverse modeling approach, such as Souri et al. (2020a), Miyazaki et al. (2020), and Souri et al. (2021), would be ideal for fully harnessing the potential of satellite information on improving multiple aspects of a model representing OH, it will be prohibitively expensive. Therefore, our simplified approach serves the purpose of understanding the first-order effects of observational adjustments to TOH drivers/proxies before committing substantial resources to the implementation/execution of an observationally-constrained, full-chemistry model. Here, we implemented the newest version of the parameterization of OH, following Anderson et al. (2022), within NASA's GEOS model, presenting an opportunity to understand and mitigate TOH biases caused by misrepresentation of HCHO and NO_2 concentrations with respect to the state-of-the-art OMI NO_2 and HCHO retrievals using Bayesian data fusion, as well as to unravel the intricacies of TOH to its key inputs such as tropospheric and stratospheric ozone and water vapor.

We found large positive biases in tropospheric NO_2 columns in M2GMI, the archived model used as an input to the parameterization of OH, compared to OMI over Africa, Eastern Europe, and the Midwest US. Because of a large positive effect of NO_2 (a surrogate for NOx) on TOH, a tendency well captured by our implicit parameterization, these overestimations introduced significant regional biases in TOH up to 20%, and a global overestimation of TOH by 1%. Consistent with former work, we saw distinct disparities in the sign of linear trends of tropospheric NO_2 over high- and medium-income countries (i.e., negative) and low-income countries (i.e., positive). While M2GMI generally replicated these trends, notable deviations were identified over China leading to an erroneous trend of TOH.

Pronounced inaccuracies with regards to both the simulated HCHO magnitude and trend in M2GMI were revealed by OMI over land. However, this proxy for OH was loosely connected to TOH in areas where photolysis was not the major sink of HCHO (Wolfe et al., 2019), especially over land. Over oceans, where HCHO and TOH were highly correlated, adjustments to M2GMI by OMI HCHO were relatively mild resulting in small alterations to TOH which was by an order of magnitude lower than those of NO_2. These mild alterations speak to either an insufficient amount of information in OMI or the reasonable accuracy of M2GMI over pristine areas.

In general, five variables including NO_2, HCHO, water vapor, tropospheric ozone, and stratospheric ozone, could collectively account for 65% of the variance in TOH trends globally. To estimate this, we executed various modeling experiments to isolate the effect of NO_2, HCHO, water vapor, tropospheric ozone, and stratospheric ozone on long-term trends of TOH in 2005-2019 at $1^o \times 1^o$ resolution. Except for tropospheric ozone, these variables were either constrained by observations or aligned with independent observations, boosting confidence in our trend results. Given the robust positive correlation between OH and NO_2, HCHO, water vapor, and tropospheric ozone over regions where photochemistry was active, TOH trends influenced by these variables closely mirrored the trends in their respective drivers/proxies. For instance, high- and medium-income countries exhibited negative TOH trends driven by NO_2. Rising tropospheric ozone over east and south Asia, heavily vetted by various observations (Guadel et al., 2018), led to an upswing in TOH over the Pacific Ocean. The trend of water vapor, greatly in agreement with independent observation (Broger et al., 2022), was dominantly positive over oceans leading to further enhancement of TOH. Rising HCHO over Pacific and Indian Ocean suggested by constrained M2GMI was associated with increased TOH. The effect of stratospheric ozone on TOH was marginal in low and mid latitudes due to negligible changes in stratospheric ozone columns in M2GMI reconfirmed by OMI total ozone column observations.

A large offset between our analysis experiment with varying CO and CH_4 concentrations was observed after removing the sum of the linear trends derived from these five key experiments from the analysis experiment, indicating that our future research using ECCOH should include new experiments isolating the effects of CO, CH_4, and transport (e.g., Gaubert et al., 2017; Zhao et al., 2020). Those experiments will refine the investigation of the unexplained portion of the TOH trend.

The development of an effective parameterization of OH, that is capable of integrating advanced satellite-based gas retrievals and improved weather forecast models enabled us to unravel the convoluted response of TOH to various parameters. Nonetheless, it is important to recognize some of the limitations

https://doi.org/10.5194/egusphere-2024-410
Preprint. Discussion started: 29 February 2024

associated with our work: the offline nature of the Bayesian data fusion algorithm makes the entire experiment blind to the interconnected responses of various compounds, such as ozone or aerosols, to adjustments to NO_2 and HCHO. Despite this limitation, our work has provided valuable insights into the first-order effects of adjustments on TOH key inputs. This can help quickly identify areas where our prior knowledge is least reliable to simulate TOH.

The longevity and stability of Aura's record of observations have played a significant role in constraining/assessing several important variables pertaining to TOH on a global scale. This is exemplified by the wealth of information obtained from OMI NO_2, HCHO, water vapor, total ozone columns, and Microwave Limb Sounding (MLS) temperature and ozone, that are used directly or indirectly in our analysis. However, as Aura's mission comes to an end, there will be a gap in the monitoring of these variables. TROPOMI, OMI's successor, can help fill this gap, but its record of observation is still short; therefore, it is important to invest in research to harmonize data from multiple satellite observations such as OMI and TROPOMI (e.g., Hilboll et al., 2013). This is because each sensor can have different biases and spatial representativity, which can lead to inconsistencies and potentially conflicting values if they are used together.

Acknowledgements

This research was supported by the National Aeronautics and Space Administration (NASA) Aura Mission project science funds. We thank Gonzalo Gonzalez Abad for sharing OMI HCHO v4 data.

Data availability

Satellite data can be accessed for Level 2 OMI tropospheric NO_2 at https://doi.org/10.5067/MEASURES/MINDS/DATA204 (Lamsal et al., 2022), Level 2 OMI total ozone columns at https://disc.gsfc.nasa.gov/datasets/OMTO3_003/summary (Bhartia, 2005), OMI SAO HCHO at https://waps.cfa.harvard.edu/sao_atmos/data/omi_hcho/OMI-HCHO-L2/ (Gonzalez Abad, 2023), MOPITT CO (https://doi.org/10.5067/TERRA/MOPITT/MOP03JM_L3.008) (NASA LARC, 2000), OMI/MLS TO_3 at https://acd-ext.gsfc.nasa.gov/Data_services/cloud_slice/data/tco_omimls.nc (Ziemke, 2023).
In-situ CO and CH_4 observations can be obtained from https://gml.noaa.gov/dv/data/index.php?category=Greenhouse%2BGases (Helmig et al., 2021; Lan et al.,2021).
MERRA2-GMI model outputs can be downloaded from https://acd-ext.gsfc.nasa.gov/Projects/GEOSCCM/MERRA2GMI/ (NASA Goddard Space Flight Center, 2023).

Code availability

OI-SAT-GMI python package developed for this research can be found from https://doi.org/10.5281/zenodo.10520136 (Souri, 2024).
GEOS-Quickchem used to run the modeling experiments encompassing ECCOH can be found from https://github.com/GEOS-ESM/QuickChem.git.
GEOS model can be obtained from https://github.com/GEOS-ESM/GEOSgcm.git.
Offline ECCOH calculations to derive the sensitivity of TOH to different drivers/proxies can be obtained from https://doi.org/10.5281/zenodo.10685100

Authors contributions

A.H.S and B.N.D designed the research. A.H.S analyzed the data, conducted the simulations, made all the figures, and wrote the original manuscript. B.N.D helped with conceptualization, fund raising, and writing. S.A.S helped configuring the model and interpreting the results. M.E.M and D.C.A implemented the improved ECCOH module into GEOS-5 Quickchem. J.L. thoroughly validated the model with respect to CO and CH_4 observations. B.W. provided an improved CO emission inventory. L.D.O provided M2GMI and helped interpret it. Z.Z. provided improved wetland CH_4 emissions. All the authors contributed to the discussion and edited the paper.

Competing interests

B.N.D is a member of the editorial board of Atmospheric Chemistry and Physics.

https://doi.org/10.5194/egusphere-2024-410
Preprint. Discussion started: 29 February 2024

References

Allan, R. P., Willett, K. M., John, V. O., and Trent, T.: Global Changes in Water Vapor 1979–2020, J. Geophys. Res. Atmos., 127, e2022JD036728, https://doi.org/10.1029/2022JD036728, 2022.

Anderson, D. C., Duncan, B. N., Fiore, A. M., Baublitz, C. B., Follette-Cook, M. B., Nicely, J. M., and Wolfe, G. M.: Spatial and temporal variability in the hydroxyl (OH) radical: understanding the role of large-scale climate features and their influence on OH through its dynamical and photochemical drivers, Atmos. Chem. Phys., 21, 6481–6508, https://doi.org/10.5194/acp-21-6481-2021, 2021.

Anderson, D. C., Duncan, B. N., Nicely, J. M., Liu, J., Strode, S. A., and Follette-Cook, M. B.: Technical note: Constraining the hydroxyl (OH) radical in the tropics with satellite observations of its drivers – first steps toward assessing the feasibility of a global observation strategy, Atmos. Chem. Phys., 23, 6319–6338, https://doi.org/10.5194/acp-23-6319-2023, 2023.

Anderson, D. C., Follette-Cook, M. B., Strode, S. A., Nicely, J. M., Liu, J., Ivatt, P. D., and Duncan, B. N.: A machine learning methodology for the generation of a parameterization of the hydroxyl radical, Geosci. Model Dev., 15, 6341–6358, https://doi.org/10.5194/gmd-15-6341-2022, 2022.

Bacmeister, J. T., Suarez, M. J., and Robertson, F. R.: Rain Reevaporation, Boundary Layer–Convection Interactions, and Pacific Rainfall Patterns in an AGCM, J. Atmos. Sci., 63, 3383–3403, https://doi.org/10.1175/JAS3791.1, 2006.

Baublitz, C. B., Fiore, A. M., Ludwig, S. M., Nicely, J. M., Wolfe, G. M., Murray, L. T., Commane, R., Prather, M. J., Anderson, D. C., Correa, G., Duncan, B. N., Follette-Cook, M., Westervelt, D. M., Bourgeois, I., Brune, W. H., Bui, T. P., DiGangi, J. P., Diskin, G. S., Hall, S. R., McKain, K., Miller, D. O., Peischl, J., Thames, A. B., Thompson, C. R., Ullmann, K., and Wofsy, S. C.: An observation-based, reduced-form model for oxidation in the remote marine troposphere, Proc. Natl. Acad. Sci., 120, e2209735120, https://doi.org/10.1073/pnas.2209735120, 2023.

Bauwens, M., Stavrakou, T., Müller, J.-F., De Smedt, I., Van Roozendael, M., van der Werf, G. R., Wiedinmyer, C., Kaiser, J. W., Sindelarova, K., and Guenther, A.: Nine years of global hydrocarbon emissions based on source inversion of OMI formaldehyde observations, Atmos. Chem. Phys., 16, 10133–10158, https://doi.org/10.5194/acp-16-10133-2016, 2016.

Bauwens, M., Verreyken, B., Stavrakou, T., Müller, J.-F., and Smedt, I. D.: Spaceborne evidence for significant anthropogenic VOC trends in Asian cities over 2005–2019, Environ. Res. Lett., 17, 015008, https://doi.org/10.1088/1748-9326/ac46eb, 2022.

Bhartia, Pawan K., (2005), OMI/Aura Ozone (O3) Total Column 1-Orbit L2 Swath 13x24 km V003, Greenbelt, MD, USA, Goddard Earth Sciences Data and Information Services Center (GES DISC), Accessed: June 2023, 10.5067/Aura/OMI/DATA2024

Bocquet, M., Elbern, H., Eskes, H., Hirtl, M., Žabkar, R., Carmichael, G. R., Flemming, J., Inness, A., Pagowski, M., Pérez Camaño, J. L., Saide, P. E., San Jose, R., Sofiev, M., Vira, J., Baklanov, A., Carnevale, C., Grell, G., and Seigneur, C.: Data assimilation in atmospheric chemistry models: current status and future prospects for coupled chemistry meteorology models, Atmos. Chem. Phys., 15, 5325–5358, https://doi.org/10.5194/acp-15-5325-2015, 2015.

Borger, C., Beirle, S., and Wagner, T.: Analysis of global trends of total column water vapour from multiple years of OMI observations, Atmos. Chem. Phys., 22, 10603–10621, https://doi.org/10.5194/acp-22-10603-2022, 2022.

Bosilovich, M. G., Robertson, F. R., Takacs, L., Molod, A., and Mocko, D.: Atmospheric Water Balance and Variability in the MERRA-2 Reanalysis, J. Clim., 30, 1177–1196, https://doi.org/10.1175/JCLI-D-16-0338.1, 2017.

Bousquet, P., Hauglustaine, D. A., Peylin, P., Carouge, C., and Ciais, P.: Two decades of OH variability as inferred by an inversion of atmospheric transport and chemistry of methyl chloroform, Atmos. Chem. Phys., 5, 2635–2656, https://doi.org/10.5194/acp-5-2635-2005, 2005.

Brune, W. H., Miller, D. O., Thames, A. B., Allen, H. M., Apel, E. C., Blake, D. R., Bui, T. P., Commane, R., Crounse, J. D., Daube, B. C., Diskin, G. S., DiGangi, J. P., Elkins, J. W., Hall, S. R., Hanisco, T. F.,

Hannun, R. A., Hintsa, E. J., Hornbrook, R. S., Kim, M. J., McKain, K., Moore, F. L., Neuman, J. A., Nicely, J. M., Peischl, J., Ryerson, T. B., St. Clair, J. M., Sweeney, C., Teng, A. P., Thompson, C., Ullmann, K., Veres, P. R., Wennberg, P. O., and Wolfe, G. M.: Exploring Oxidation in the Remote Free Troposphere: Insights From Atmospheric Tomography (ATom), J. Geophys. Res. Atmos., 125, e2019JD031685, https://doi.org/10.1029/2019JD031685, 2020.

Brune, W. H., Miller, D. O., Thames, A. B., Brosius, A. L., Barletta, B., Blake, D. R., Blake, N. J., Chen, G., Choi, Y., Crawford, J. H., Digangi, J. P., Diskin, G., Fried, A., Hall, S. R., Hanisco, T. F., Huey, G. L., Hughes, S. C., Kim, M., Meinardi, S., Montzka, D. D., Pusede, S. E., Schroeder, J. R., Teng, A., Tanner, D. J., Ullmann, K., Walega, J., Weinheimer, A., Wisthaler, A., and Wennberg, P. O.: Observations of atmospheric oxidation and ozone production in South Korea, Atmos. Environ., 269, 118854, https://doi.org/10.1016/j.atmosenv.2021.118854, 2022.

Canty, T. P., Hembeck, L., Vinciguerra, T. P., Anderson, D. C., Goldberg, D. L., Carpenter, S. F., Allen, D. J., Loughner, C. P., Salawitch, R. J., and Dickerson, R. R.: Ozone and NOx chemistry in the eastern US: evaluation of CMAQ/CB05 with satellite (OMI) data, Atmos. Chem. Phys., 15, 10965–10982, https://doi.org/10.5194/acp-15-10965-2015, 2015.

Chen, B. and Liu, Z.: Global water vapor variability and trend from the latest 36 year (1979 to 2014) data of ECMWF and NCEP reanalyses, radiosonde, GPS, and microwave satellite, J. Geophys. Res. Atmos., 121, 11,442-11,462, https://doi.org/10.1002/2016JD024917, 2016.

Chin, M., Ginoux, P., Kinne, S., Torres, O., Holben, B. N., Duncan, B. N., Martin, R. V., Logan, J. A., Higurashi, A., and Nakajima, T.: Tropospheric Aerosol Optical Thickness from the GOCART Model and Comparisons with Satellite and Sun Photometer Measurements, J. Atmos. Sci., 59, 461–483, https://doi.org/10.1175/1520-0469(2002)059<0461:TAOTFT>2.0.CO;2, 2002.

Choi, S., Lamsal, L. N., Follette-Cook, M., Joiner, J., Krotkov, N. A., Swartz, W. H., Pickering, K. E., Loughner, C. P., Appel, W., Pfister, G., Saide, P. E., Cohen, R. C., Weinheimer, A. J., and Herman, J. R.: Assessment of NO2 observations during DISCOVER-AQ and KORUS-AQ field campaigns, Atmos. Meas. Tech., 13, 2523–2546, https://doi.org/10.5194/amt-13-2523-2020, 2020.

Choi, Y. and Souri, A. H.: Chemical condition and surface ozone in large cities of Texas during the last decade: Observational evidence from OMI, CAMS, and model analysis, Remote Sens. Environ., 168, 90–101, https://doi.org/10.1016/j.rse.2015.06.026, 2015a.

Choi, Y. and Souri, A. H.: Seasonal behavior and long-term trends of tropospheric ozone, its precursors and chemical conditions over Iran: A view from space, Atmos. Environ., 106, 232–240, https://doi.org/10.1016/j.atmosenv.2015.02.012, 2015b.

Chua, G., Naik, V., and Horowitz, L. W.: Exploring the drivers of tropospheric hydroxyl radical trends in the Geophysical Fluid Dynamics Laboratory AM4.1 atmospheric chemistry–climate model, Atmos. Chem. Phys., 23, 4955–4975, https://doi.org/10.5194/acp-23-4955-2023, 2023.

Cox, C. and Munk, W.: Measurement of the Roughness of the Sea Surface from Photographs of the Sun's Glitter, J. Opt. Soc. Am., JOSA, 44, 838–850, https://doi.org/10.1364/JOSA.44.000838, 1954.

Crippa, M., Guizzardi, D., Muntean, M., Schaaf, E., Vullo, E. L., Solazzo, E., Monforti-Ferrario, F., Olivier, J., and Vignati, E.: EDGAR v5.0 Greenhouse Gas Emissions, 2019.

de Foy, B., Lu, Z., and Streets, D. G.: Satellite NO2 retrievals suggest China has exceeded its NOx reduction goals from the twelfth Five-Year Plan, Sci. Rep., 6, 35912, https://doi.org/10.1038/srep35912, 2016.

De Smedt, I., Stavrakou, T., Hendrick, F., Danckaert, T., Vlemmix, T., Pinardi, G., Theys, N., Lerot, C., Gielen, C., Vigouroux, C., Hermans, C., Fayt, C., Veefkind, P., Müller, J.-F., and Van Roozendael, M.: Diurnal, seasonal and long-term variations of global formaldehyde columns inferred from combined OMI and GOME-2 observations, Atmos. Chem. Phys., 15, 12519–12545, https://doi.org/10.5194/acp-15-12519-2015, 2015.

Dhame, S., Taschetto, A. S., Santoso, A., and Meissner, K. J.: Indian Ocean warming modulates global atmospheric circulation trends, Clim. Dyn., 55, 2053–2073, https://doi.org/10.1007/s00382-020-05369-1, 2020.

Duncan, B. N., Lamsal, L. N., Thompson, A. M., Yoshida, Y., Lu, Z., Streets, D. G., Hurwitz, M. M., and Pickering, K. E.: A space-based, high-resolution view of notable changes in urban NOx pollution

https://doi.org/10.5194/egusphere-2024-410
Preprint. Discussion started: 29 February 2024

around the world (2005–2014), J. Geophys. Res. Atmos., 121, 976–996, https://doi.org/10.1002/2015JD024121, 2016.

Duncan, B. N., Logan, J. A., Bey, I., Megretskaia, I. A., Yantosca, R. M., Novelli, P. C., Jones, N. B., and Rinsland, C. P.: Global budget of CO, 1988–1997: Source estimates and validation with a global model, J. Geophys. Res. Atmos., 112, https://doi.org/10.1029/2007JD008459, 2007b.

Duncan, B. N., Strahan, S. E., Yoshida, Y., Steenrod, S. D., and Livesey, N.: Model study of the cross-tropopause transport of biomass burning pollution, Atmos. Chem. Phys., 7, 3713–3736, https://doi.org/10.5194/acp-7-3713-2007, 2007a.

Duncan, B. N., Yoshida, Y., Damon, M. R., Douglass, A. R., and Witte, J. C.: Temperature dependence of factors controlling isoprene emissions, Geophys. Res. Lett., 36, https://doi.org/10.1029/2008GL037090, 2009.

Duncan, B., Portman, D., Bey, I., and Spivakovsky, C.: Parameterization of OH for efficient computation in chemical tracer models, J. Geophys. Res. Atmos, 105, 12259–12262, https://doi.org/10.1029/1999JD901141, 2000.

Edwards, D. P., Lamarque, J.-F., Attié, J.-L., Emmons, L. K., Richter, A., Cammas, J.-P., Gille, J. C., Francis, G. L., Deeter, M. N., Warner, J., Ziskin, D. C., Lyjak, L. V., Drummond, J. R., and Burrows, J. P.: Tropospheric ozone over the tropical Atlantic: A satellite perspective, J. Geophys. Res. Atmos., 108, https://doi.org/10.1029/2002JD002927, 2003.

Elshorbany, Y. F., Duncan, B. N., Strode, S. A., Wang, J. S., and Kouatchou, J.: The description and validation of the computationally Efficient CH4–CO–OH (ECCOHv1.01) chemistry module for 3-D model applications, Geosci. Model Dev., 9, 799–822, https://doi.org/10.5194/gmd-9-799-2016, 2016.

Fasnacht, Z., Vasilkov, A., Haffner, D., Qin, W., Joiner, J., Krotkov, N., Sayer, A. M., and Spurr, R.: A geometry-dependent surface Lambertian-equivalent reflectivity product for UV–Vis retrievals – Part 2: Evaluation over open ocean, Atmos. Meas. Tech., 12, 6749–6769, https://doi.org/10.5194/amt-12-6749-2019, 2019.

Ferrario, F. M., Crippa, M., Guizzardi, D., Muntean, M., Schaaf, E., Vullo, E. L., Solazzo, E., Olivier, J., and Vignati, E.: EDGAR v6.0 Greenhouse Gas Emissions, 2021.

Fiore, A. M., Mickley, L. J., Zhu, Q., and Baublitz, C. B.: Climate and Tropospheric Oxidizing Capacity, Annu. Rev. Earth. Planet. Sci. , 52, null, https://doi.org/10.1146/annurev-earth-032320-090307, 2024.

Gaubert, B., Worden, H. M., Arellano, A. F. J., Emmons, L. K., Tilmes, S., Barré, J., Martinez Alonso, S., Vitt, F., Anderson, J. L., Alkemade, F., Houweling, S., and Edwards, D. P.: Chemical Feedback From Decreasing Carbon Monoxide Emissions, Geophys. Res. Lett., 44, 9985–9995, https://doi.org/10.1002/2017GL074987, 2017.

Gaudel, A., Cooper, O. R., Ancellet, G., Barret, B., Boynard, A., Burrows, J. P., Clerbaux, C., Coheur, P.-F., Cuesta, J., Cuevas, E., Doniki, S., Dufour, G., Ebojie, F., Foret, G., Garcia, O., Granados-Muñoz, M. J., Hannigan, J. W., Hase, F., Hassler, B., Huang, G., Hurtmans, D., Jaffe, D., Jones, N., Kalabokas, P., Kerridge, B., Kulawik, S., Latter, B., Leblanc, T., Le Flochmoën, E., Lin, W., Liu, J., Liu, X., Mahieu, E., McClure-Begley, A., Neu, J. L., Osman, M., Palm, M., Petetin, H., Petropavlovskikh, I., Querel, R., Rahpoe, N., Rozanov, A., Schultz, M. G., Schwab, J., Siddans, R., Smale, D., Steinbacher, M., Tanimoto, H., Tarasick, D. W., Thouret, V., Thompson, A. M., Trickl, T., Weatherhead, E., Wespes, C., Worden, H. M., Vigouroux, C., Xu, X., Zeng, G., and Ziemke, J.: Tropospheric Ozone Assessment Report: Present-day distribution and trends of tropospheric ozone relevant to climate and global atmospheric chemistry model evaluation, Elem. Sci. Anth., 6, 39, https://doi.org/10.1525/elementa.291, 2018.

Gelaro, R., McCarty, W., Suárez, M. J., Todling, R., Molod, A., Takacs, L., Randles, C. A., Darmenov, A., Bosilovich, M. G., Reichle, R., Wargan, K., Coy, L., Cullather, R., Draper, C., Akella, S., Buchard, V., Conaty, A., Silva, A. M. da, Gu, W., Kim, G.-K., Koster, R., Lucchesi, R., Merkova, D., Nielsen, J. E., Partyka, G., Pawson, S., Putman, W., Rienecker, M., Schubert, S. D., Sienkiewicz, M., and Zhao, B.: The Modern-Era Retrospective Analysis for Research and Applications, Version 2 (MERRA-2), J. Clim., 30, 5419–5454, https://doi.org/10.1175/JCLI-D-16-0758.1, 2017.

https://doi.org/10.5194/egusphere-2024-410
Preprint. Discussion started: 29 February 2024

Giglio, L., Randerson, J. T., and van der Werf, G. R.: Analysis of daily, monthly, and annual burned area using the fourth-generation global fire emissions database (GFED4), J. Geophys. Res. Biogeosci., 118, 317–328, https://doi.org/10.1002/jgrg.20042, 2013.

Gonzalez Abad, (2003), OMI SAO HCHO Total Column L2 Swath V4, Cambridge, MA, USA, Accessed: May 2023, https://waps.cfa.harvard.edu/sao_atmos/data/omi_hcho/OMI-HCHO-L2/

González Abad, G., Liu, X., Chance, K., Wang, H., Kurosu, T. P., and Suleiman, R.: Updated Smithsonian Astrophysical Observatory Ozone Monitoring Instrument (SAO OMI) formaldehyde retrieval, Atmos. Meas. Tech., 8, 19–32, https://doi.org/10.5194/amt-8-19-2015, 2015.

Hassler, B., McDonald, B. C., Frost, G. J., Borbon, A., Carslaw, D. C., Civerolo, K., Granier, C., Monks, P. S., Monks, S., Parrish, D. D., Pollack, I. B., Rosenlof, K. H., Ryerson, T. B., von Schneidemesser, E., and Trainer, M.: Analysis of long-term observations of NOx and CO in megacities and application to constraining emissions inventories, Geophys. Res. Lett., 43, 9920–9930, https://doi.org/10.1002/2016GL069894, 2016.

He, J., Naik, V., and Horowitz, L. W.: Hydroxyl Radical (OH) Response to Meteorological Forcing and Implication for the Methane Budget, Geophys. Res. Lett., 48, e2021GL094140, https://doi.org/10.1029/2021GL094140, 2021.

Helmig, D., Hueber, J., Tans, P., University Of Colorado Institute Of Arctic And Alpine Research (INSTAAR), & NOAA GML CCGG Group. (2021). University of Colorado Institute of Arctic and Alpine Research (INSTAAR) Flask-Air Sample Measurements of Atmospheric Non Methane Hydrocarbons Mole Fractions from the NOAA GML Carbon Cycle Surface Network at Global and Regional Background Sites, 2004-2016 (Version 2021.05.04) [Data set]. NOAA Global Monitoring Laboratory. https://doi.org/10.15138/6AV8-GS57

Hickman, J. E., Andela, N., Tsigaridis, K., Galy-Lacaux, C., Ossohou, M., and Bauer, S. E.: Reductions in NO2 burden over north equatorial Africa from decline in biomass burning in spite of growing fossil fuel use, 2005 to 2017, Proc. Natl. Acad. Sci., 118, e2002579118, https://doi.org/10.1073/pnas.2002579118, 2021.

Hilboll, A., Richter, A., and Burrows, J. P.: Long-term changes of tropospheric NO2 over megacities derived from multiple satellite instruments, Atmos. Chem. Phys., 13, 4145–4169, https://doi.org/10.5194/acp-13-4145-2013, 2013.

Holmes, C. D., Prather, M. J., Søvde, O. A., and Myhre, G.: Future methane, hydroxyl, and their uncertainties: key climate and emission parameters for future predictions, Atmos. Chem. Phys., 13, 285–302, https://doi.org/10.5194/acp-13-285-2013, 2013.

Hudman, R. C., Moore, N. E., Mebust, A. K., Martin, R. V., Russell, A. R., Valin, L. C., and Cohen, R. C.: Steps towards a mechanistic model of global soil nitric oxide emissions: implementation and space based-constraints, Atmos. Chem. Phys., 12, 7779–7795, https://doi.org/10.5194/acp-12-7779-2012, 2012.

Jaeglé, L., Steinberger, L., V. Martin, R., and Chance, K.: Global partitioning of NO x sources using satellite observations: Relative roles of fossil fuel combustion , biomass burning and soil emissions, Faraday Discuss., 130, 407–423, https://doi.org/10.1039/B502128F, 2005.

Jin, X. and Holloway, T.: Spatial and temporal variability of ozone sensitivity over China observed from the Ozone Monitoring Instrument, J. Geophys. Res. Atmos., 120, 7229–7246, https://doi.org/10.1002/2015JD023250, 2015.

Jones, M. W., Abatzoglou, J. T., Veraverbeke, S., Andela, N., Lasslop, G., Forkel, M., Smith, A. J. P., Burton, C., Betts, R. A., van der Werf, G. R., Sitch, S., Canadell, J. G., Santín, C., Kolden, C., Doerr, S. H., and Le Quéré, C.: Global and Regional Trends and Drivers of Fire Under Climate Change, Rev. Geophys., 60, e2020RG000726, https://doi.org/10.1029/2020RG000726, 2022.

Jung, J., Souri, A. H., Wong, D. C., Lee, S., Jeon, W., Kim, J., and Choi, Y.: The Impact of the Direct Effect of Aerosols on Meteorology and Air Quality Using Aerosol Optical Depth Assimilation During the KORUS-AQ Campaign, J. Geophys. Res. Atmos, 124, 8303–8319, https://doi.org/10.1029/2019JD030641, 2019.

https://doi.org/10.5194/egusphere-2024-410
Preprint. Discussion started: 29 February 2024

Krotkov, N. A., McLinden, C. A., Li, C., Lamsal, L. N., Celarier, E. A., Marchenko, S. V., Swartz, W. H., Bucsela, E. J., Joiner, J., Duncan, B. N., Boersma, K. F., Veefkind, J. P., Levelt, P. F., Fioletov, V. E., Dickerson, R. R., He, H., Lu, Z., and Streets, D. G.: Aura OMI observations of regional SO2 and NO2 pollution changes from 2005 to 2015, Atmos. Chem. Phys., 16, 4605–4629, https://doi.org/10.5194/acp-16-4605-2016, 2016.

Kuttippurath, J., Abbhishek, K., Gopikrishnan, G. S., and Pathak, M.: Investigation of long–term trends and major sources of atmospheric HCHO over India, Environ. Chall., 7, 100477, https://doi.org/10.1016/j.envc.2022.100477, 2022.

Kwon, H.-A., Abad, G. G., Nowlan, C. R., Chong, H., Souri, A. H., Vigouroux, C., Röhling, A., Kivi, R., Makarova, M., Notholt, J., Palm, M., Winkler, H., Té, Y., Sussmann, R., Rettinger, M., Mahieu, E., Strong, K., Lutsch, E., Yamanouchi, S., Nagahama, T., Hannigan, J. W., Zhou, M., Murata, I., Grutter, M., Stremme, W., De Mazière, M., Jones, N., Smale, D., and Morino, I.: Validation of OMPS Suomi NPP and OMPS NOAA-20 Formaldehyde Total Columns With NDACC FTIR Observations, Earth Space Sci., 10, e2022EA002778, https://doi.org/10.1029/2022EA002778, 2023.

Lamsal, L. N., Duncan, B. N., Yoshida, Y., Krotkov, N. A., Pickering, K. E., Streets, D. G., and Lu, Z.: U.S. NO2 trends (2005–2013): EPA Air Quality System (AQS) data versus improved observations from the Ozone Monitoring Instrument (OMI), Atmos. Environ., 110, 130–143, https://doi.org/10.1016/j.atmosenv.2015.03.055, 2015.

Lamsal, L. N., Krotkov, N. A., Vasilkov, A., Marchenko, S., Qin, W., Yang, E.-S., Fasnacht, Z., Joiner, J., Choi, S., Haffner, D., Swartz, W. H., Fisher, B., and Bucsela, E.: Ozone Monitoring Instrument (OMI) Aura nitrogen dioxide standard product version 4.0 with improved surface and cloud treatments, Atmos. Meas. Tech., 14, 455–479, https://doi.org/10.5194/amt-14-455-2021, 2021.

Lamsal, Lok N., Nickolay A. Krotkov, Sergey V. Marchenko, Joanna Joiner, Luke Oman, Alexander Vasilkov, Bradford Fisher, Wenhan Qin, Eun-Su Yang, Zachary Fasnacht, Sungyeon Choi, Peter Leonard, and David Haffner (2022), OMI/Aura NO2 Tropospheric, Stratospheric & Total Columns MINDS 1-Orbit L2 Swath 13 kmx24 km, NASA Goddard Space Flight Center, Goddard Earth Sciences Data and Information Services Center (GES DISC), Accessed: May 2023, 10.5067/MEASURES/MINDS/DATA204

Lan, X., J.W. Mund, A.M. Crotwell, M.J. Crotwell, E. Moglia, M. Madronich, D. Neff and K.W. Thoning (2023), Atmospheric Methane Dry Air Mole Fractions from the NOAA GML Carbon Cycle Cooperative Global Air Sampling Network, 1983-2022, Version: 2023-08-28, https://doi.org/10.15138/VNCZ-M766

Lawrence, M. G., Jöckel, P., and von Kuhlmann, R.: What does the global mean OH concentration tell us?, Atmos. Chem. Phys., 1, 37–49, https://doi.org/10.5194/acp-1-37-2001, 2001.

Lelieveld, J., Gromov, S., Pozzer, A., and Taraborrelli, D.: Global tropospheric hydroxyl distribution, budget and reactivity, Atmos. Chem. Phys., 16, 12477–12493, https://doi.org/10.5194/acp-16-12477-2016, 2016.

Lin, M., Horowitz, L. W., Payton, R., Fiore, A. M., and Tonnesen, G.: US surface ozone trends and extremes from 1980 to 2014: quantifying the roles of rising Asian emissions, domestic controls, wildfires, and climate, Atmos. Chem. Phys., 17, 2943–2970, https://doi.org/10.5194/acp-17-2943-2017, 2017.

Marais, E. A., Jacob, D. J., Kurosu, T. P., Chance, K., Murphy, J. G., Reeves, C., Mills, G., Casadio, S., Millet, D. B., Barkley, M. P., Paulot, F., and Mao, J.: Isoprene emissions in Africa inferred from OMI observations of formaldehyde columns, Atmos. Chem. Phys., 12, 6219–6235, https://doi.org/10.5194/acp-12-6219-2012, 2012.

Miller, D. O. and Brune, W. H.: Investigating the Understanding of Oxidation Chemistry Using 20 Years of Airborne OH and HO2 Observations, J. Geophys. Res. Atmos., 127, e2021JD035368, https://doi.org/10.1029/2021JD035368, 2022.

Millet, D. B., Jacob, D. J., Boersma, K. F., Fu, T.-M., Kurosu, T. P., Chance, K., Heald, C. L., and Guenther, A.: Spatial distribution of isoprene emissions from North America derived from formaldehyde column measurements by the OMI satellite sensor, J. Geophys. Res. Atmos., 113, https://doi.org/10.1029/2007JD008950, 2008.

https://doi.org/10.5194/egusphere-2024-410
Preprint. Discussion started: 29 February 2024

Miyazaki, K., Bowman, K. W., Yumimoto, K., Walker, T., and Sudo, K.: Evaluation of a multi-model, multi-constituent assimilation framework for tropospheric chemical reanalysis, Atmos. Chem. Phys., 20, 931–967, https://doi.org/10.5194/acp-20-931-2020, 2020.

Molod, A., Takacs, L., Suarez, M., and Bacmeister, J.: Development of the GEOS-5 atmospheric general circulation model: evolution from MERRA to MERRA2, Geosci. Model Dev., 8, 1339–1356, https://doi.org/10.5194/gmd-8-1339-2015, 2015.

Moorthi, S. and Suarez, M. J.: Relaxed Arakawa-Schubert. A Parameterization of Moist Convection for General Circulation Models, Mon. Weather Rev., 120, 978–1002, https://doi.org/10.1175/1520-0493(1992)120<0978:RASAPO>2.0.CO;2, 1992.

Murray, L. T., Fiore, A. M., Shindell, D. T., Naik, V., and Horowitz, L. W.: Large uncertainties in global hydroxyl projections tied to fate of reactive nitrogen and carbon, Proc. Natl. Acad. Sci., 118, e2115204118, https://doi.org/10.1073/pnas.2115204118, 2021.

Murray, L. T., Logan, J. A., and Jacob, D. J.: Interannual variability in tropical tropospheric ozone and OH: The role of lightning, J. Geophys. Res. Atmos., 118, 11,468-11,480, https://doi.org/10.1002/jgrd.50857, 2013.

Naik, V., Voulgarakis, A., Fiore, A. M., Horowitz, L. W., Lamarque, J.-F., Lin, M., Prather, M. J., Young, P. J., Bergmann, D., Cameron-Smith, P. J., Cionni, I., Collins, W. J., Dalsøren, S. B., Doherty, R., Eyring, V., Faluvegi, G., Folberth, G. A., Josse, B., Lee, Y. H., MacKenzie, I. A., Nagashima, T., van Noije, T. P. C., Plummer, D. A., Righi, M., Rumbold, S. T., Skeie, R., Shindell, D. T., Stevenson, D. S., Strode, S., Sudo, K., Szopa, S., and Zeng, G.: Preindustrial to present-day changes in tropospheric hydroxyl radical and methane lifetime from the Atmospheric Chemistry and Climate Model Intercomparison Project (ACCMIP), Atmos. Chem. Phys., 13, 5277–5298, https://doi.org/10.5194/acp-13-5277-2013, 2013.

Naimark, J. G., Fiore, A. M., Jin, X., Wang, Y., Klovenski, E., and Braneon, C.: Evaluating Drought Responses of Surface Ozone Precursor Proxies: Variations With Land Cover Type, Precipitation, and Temperature, Geophys. Res. Lett., 48, e2020GL091520, https://doi.org/10.1029/2020GL091520, 2021.

NASA Goddard Space Flight Center: MERRA2 GMI, NASA, https://acd-445 ext.gsfc.nasa.gov/Projects/GEOSCCM/MERRA2GMI/, last access: 12 Feb. 2023.

NASA LARC. (2000) MOPITT CO gridded monthly means (Near and Thermal Infrared Radiances) V008, NASA Langley Atmospheric Science Data Center DAAC, https://doi.org/10.5067/TERRA/MOPITT/MOP03JM_L3.008

Naus, S., Montzka, S. A., Pandey, S., Basu, S., Dlugokencky, E. J., and Krol, M.: Constraints and biases in a tropospheric two-box model of OH, Atmos. Chem. Phys., 19, 407–424, https://doi.org/10.5194/acp-19-407-2019, 2019.

Nguyen, N. H., Turner, A. J., Yin, Y., Prather, M. J., and Frankenberg, C.: Effects of Chemical Feedbacks on Decadal Methane Emissions Estimates, Geophys. Res. Lett., 47, e2019GL085706, https://doi.org/10.1029/2019GL085706, 2020.

Nicely, J. M., Canty, T. P., Manyin, M., Oman, L. D., Salawitch, R. J., Steenrod, S. D., Strahan, S. E., and Strode, S. A.: Changes in Global Tropospheric OH Expected as a Result of Climate Change Over the Last Several Decades, J. Geophys. Res. Atmos, 123, 10,774-10,795, https://doi.org/10.1029/2018JD028388, 2018.

Nicely, J. M., Duncan, B. N., Hanisco, T. F., Wolfe, G. M., Salawitch, R. J., Deushi, M., Haslerud, A. S., Jöckel, P., Josse, B., Kinnison, D. E., Klekociuk, A., Manyin, M. E., Marécal, V., Morgenstern, O., Murray, L. T., Myhre, G., Oman, L. D., Pitari, G., Pozzer, A., Quaglia, I., Revell, L. E., Rozanov, E., Stenke, A., Stone, K., Strahan, S., Tilmes, S., Tost, H., Westervelt, D. M., and Zeng, G.: A machine learning examination of hydroxyl radical differences among model simulations for CCMI-1, Atmos. Chem. Phys., 20, 1341–1361, https://doi.org/10.5194/acp-20-1341-2020, 2020.

Nielsen, J. E., Pawson, S., Molod, A., Auer, B., da Silva, A. M., Douglass, A. R., Duncan, B., Liang, Q., Manyin, M., Oman, L. D., Putman, W., Strahan, S. E., and Wargan, K.: Chemical Mechanisms and

https://doi.org/10.5194/egusphere-2024-410
Preprint. Discussion started: 29 February 2024

Their Applications in the Goddard Earth Observing System (GEOS) Earth System Model, J. Adv. Model. Earth Syst., 9, 3019–3044, https://doi.org/10.1002/2017MS001011, 2017.

Nowlan, C. R., González Abad, G., Kwon, H.-A., Ayazpour, Z., Chan Miller, C., Chance, K., Chong, H., Liu, X., O'Sullivan, E., Wang, H., Zhu, L., De Smedt, I., Jaross, G., Seftor, C., and Sun, K.: Global Formaldehyde Products From the Ozone Mapping and Profiler Suite (OMPS) Nadir Mappers on Suomi NPP and NOAA-20, Earth Space Sci., 10, e2022EA002643, https://doi.org/10.1029/2022EA002643, 2023.

Orbe, C., Oman, L. D., Strahan, S. E., Waugh, D. W., Pawson, S., Takacs, L. L., and Molod, A. M.: Large-Scale Atmospheric Transport in GEOS Replay Simulations, J. Adv. Model. Earth Syst., 9, 2545–2560, https://doi.org/10.1002/2017MS001053, 2017.

Parrish, D. F. and Derber, J. C.: The National Meteorological Center's Spectral Statistical-Interpolation Analysis System, Mon. Weather Rev., 120, 1747–1763, https://doi.org/10.1175/1520-0493(1992)120<1747:TNMCSS>2.0.CO;2, 1992.

Patra, P. K., Krol, M. C., Montzka, S. A., Arnold, T., Atlas, E. L., Lintner, B. R., Stephens, B. B., Xiang, B., Elkins, J. W., Fraser, P. J., Ghosh, A., Hintsa, E. J., Hurst, D. F., Ishijima, K., Krummel, P. B., Miller, B. R., Miyazaki, K., Moore, F. L., Mühle, J., O'Doherty, S., Prinn, R. G., Steele, L. P., Takigawa, M., Wang, H. J., Weiss, R. F., Wofsy, S. C., and Young, D.: Observational evidence for interhemispheric hydroxyl-radical parity, Nature, 513, 219–223, https://doi.org/10.1038/nature13721, 2014.

Pinardi, G., Van Roozendael, M., Hendrick, F., Theys, N., Abuhassan, N., Bais, A., Boersma, F., Cede, A., Chong, J., Donner, S., Drosoglou, T., Dzhola, A., Eskes, H., Frieß, U., Granville, J., Herman, J. R., Holla, R., Hovila, J., Irie, H., Kanaya, Y., Karagkiozidis, D., Kouremeti, N., Lambert, J.-C., Ma, J., Peters, E., Piters, A., Postylyakov, O., Richter, A., Remmers, J., Takashima, H., Tiefengraber, M., Valks, P., Vlemmix, T., Wagner, T., and Wittrock, F.: Validation of tropospheric NO2 column measurements of GOME-2A and OMI using MAX-DOAS and direct sun network observations, Atmos. Meas. Tech., 13, 6141–6174, https://doi.org/10.5194/amt-13-6141-2020, 2020.

Qin, W., Fasnacht, Z., Haffner, D., Vasilkov, A., Joiner, J., Krotkov, N., Fisher, B., and Spurr, R.: A geometry-dependent surface Lambertian-equivalent reflectivity product for UV–Vis retrievals – Part 1: Evaluation over land surfaces using measurements from OMI at 466 nm, Atmos. Meas. Tech., 12, 3997–4017, https://doi.org/10.5194/amt-12-3997-2019, 2019.

Ren, X., Olson, J. R., Crawford, J. H., Brune, W. H., Mao, J., Long, R. B., Chen, Z., Chen, G., Avery, M. A., Sachse, G. W., Barrick, J. D., Diskin, G. S., Huey, L. G., Fried, A., Cohen, R. C., Heikes, B., Wennberg, P. O., Singh, H. B., Blake, D. R., and Shetter, R. E.: HOx chemistry during INTEX-A 2004: Observation, model calculation, and comparison with previous studies, J. Geophys. Res. Atmos, 113, https://doi.org/10.1029/2007JD009166, 2008.

Reuter, M., Buchwitz, M., Hilboll, A., Richter, A., Schneising, O., Hilker, M., Heymann, J., Bovensmann, H., and Burrows, J. P.: Decreasing emissions of NOx relative to CO2 in East Asia inferred from satellite observations, Nature Geosci., 7, 792–795, https://doi.org/10.1038/ngeo2257, 2014.

Rigby, M., Montzka, S. A., Prinn, R. G., White, J. W. C., Young, D., O'Doherty, S., Lunt, M. F., Ganesan, A. L., Manning, A. J., Simmonds, P. G., Salameh, P. K., Harth, C. M., Mühle, J., Weiss, R. F., Fraser, P. J., Steele, L. P., Krummel, P. B., McCulloch, A., and Park, S.: Role of atmospheric oxidation in recent methane growth, Proc. Natl. Acad. Sci., 114, 5373–5377, https://doi.org/10.1073/pnas.1616426114, 2017.

Rodgers, C. D.: Inverse Methods for Atmospheric Sounding: Theory and Practice, WORLD SCIENTIFIC, Oxford, 2000.

Sandu, A. and Chai, T.: Chemical Data Assimilation—An Overview, Atm., 2, 426–463, https://doi.org/10.3390/atmos2030426, 2011.

Saunois, M., Stavert, A. R., Poulter, B., Bousquet, P., Canadell, J. G., Jackson, R. B., Raymond, P. A., Dlugokencky, E. J., Houweling, S., Patra, P. K., Ciais, P., Arora, V. K., Bastviken, D., Bergamaschi, P., Blake, D. R., Brailsford, G., Bruhwiler, L., Carlson, K. M., Carrol, M., Castaldi, S., Chandra, N., Crevoisier, C., Crill, P. M., Covey, K., Curry, C. L., Etiope, G., Frankenberg, C., Gedney, N., Hegglin, M. I., Höglund-Isaksson, L., Hugelius, G., Ishizawa, M., Ito, A., Janssens-Maenhout, G., Jensen, K.

M., Joos, F., Kleinen, T., Krummel, P. B., Langenfelds, R. L., Laruelle, G. G., Liu, L., Machida, T., Maksyutov, S., McDonald, K. C., McNorton, J., Miller, P. A., Melton, J. R., Morino, I., Müller, J., Murguia-Flores, F., Naik, V., Niwa, Y., Noce, S., O'Doherty, S., Parker, R. J., Peng, C., Peng, S., Peters, G. P., Prigent, C., Prinn, R., Ramonet, M., Regnier, P., Riley, W. J., Rosentreter, J. A., Segers, A., Simpson, I. J., Shi, H., Smith, S. J., Steele, L. P., Thornton, B. F., Tian, H., Tohjima, Y., Tubiello, F. N., Tsuruta, A., Viovy, N., Voulgarakis, A., Weber, T. S., van Weele, M., van der Werf, G. R., Weiss, R. F., Worthy, D., Wunch, D., Yin, Y., Yoshida, Y., Zhang, W., Zhang, Z., Zhao, Y., Zheng, B., Zhu, Q., Zhu, Q., and Zhuang, Q.: The Global Methane Budget 2000–2017, Earth Syst. Sci. Data., 12, 1561–1623, https://doi.org/10.5194/essd-12-1561-2020, 2020.

Shen, L., Jacob, D. J., Zhu, L., Zhang, Q., Zheng, B., Sulprizio, M. P., Li, K., De Smedt, I., González Abad, G., Cao, H., Fu, T.-M., and Liao, H.: The 2005–2016 Trends of Formaldehyde Columns Over China Observed by Satellites: Increasing Anthropogenic Emissions of Volatile Organic Compounds and Decreasing Agricultural Fire Emissions, Geophys. Res. Lett., 46, 4468–4475, https://doi.org/10.1029/2019GL082172, 2019.

Souri, A. H., Chance, K., Bak, J., Nowlan, C. R., González Abad, G., Jung, Y., Wong, D. C., Mao, J., and Liu, X.: Unraveling pathways of elevated ozone induced by the 2020 lockdown in Europe by an observationally constrained regional model using TROPOMI, Atmos. Chem. Phys., 21, 18227–18245, https://doi.org/10.5194/acp-21-18227-2021, 2021.

Souri, A. H., Choi, Y., Jeon, W., Li, X., Pan, S., Diao, L., and Westenbarger, D. A.: Constraining NOx emissions using satellite NO2 measurements during 2013 DISCOVER-AQ Texas campaign, Atmos. Environ., 131, 371–381, https://doi.org/10.1016/j.atmosenv.2016.02.020, 2016.

Souri, A. H., Choi, Y., Jeon, W., Woo, J.-H., Zhang, Q., and Kurokawa, J.: Remote sensing evidence of decadal changes in major tropospheric ozone precursors over East Asia, J. Geophys. Res. Atmos., 122, 2474–2492, https://doi.org/10.1002/2016JD025663, 2017.

Souri, A. H., Choi, Y., Kodros, J. K., Jung, J., Shpund, J., Pierce, J. R., Lynn, B. H., Khain, A., and Chance, K.: Response of Hurricane Harvey's rainfall to anthropogenic aerosols: A sensitivity study based on spectral bin microphysics with simulated aerosols, Atmos. Res., 242, 104965, https://doi.org/10.1016/j.atmosres.2020.104965, 2020b.

Souri, A. H., Johnson, M. S., Wolfe, G. M., Crawford, J. H., Fried, A., Wisthaler, A., Brune, W. H., Blake, D. R., Weinheimer, A. J., Verhoelst, T., Compernolle, S., Pinardi, G., Vigouroux, C., Langerock, B., Choi, S., Lamsal, L., Zhu, L., Sun, S., Cohen, R. C., Min, K.-E., Cho, C., Philip, S., Liu, X., and Chance, K.: Characterization of errors in satellite-based HCHO / NO2 tropospheric column ratios with respect to chemistry, column-to-PBL translation, spatial representation, and retrieval uncertainties, Atmos. Chem. Phys., 23, 1963–1986, https://doi.org/10.5194/acp-23-1963-2023, 2023.

Souri, A. H., Nowlan, C. R., González Abad, G., Zhu, L., Blake, D. R., Fried, A., Weinheimer, A. J., Wisthaler, A., Woo, J.-H., Zhang, Q., Chan Miller, C. E., Liu, X., and Chance, K.: An inversion of NOx and non-methane volatile organic compound (NMVOC) emissions using satellite observations during the KORUS-AQ campaign and implications for surface ozone over East Asia, Atmos. Chem. Phys., 20, 9837–9854, https://doi.org/10.5194/acp-20-9837-2020, 2020a.

Souri, A. H., Nowlan, C. R., Wolfe, G. M., Lamsal, L. N., Chan Miller, C. E., Abad, G. G., Janz, S. J., Fried, A., Blake, D. R., Weinheimer, A. J., Diskin, G. S., Liu, X., and Chance, K.: Revisiting the effectiveness of HCHO/NO2 ratios for inferring ozone sensitivity to its precursors using high resolution airborne remote sensing observations in a high ozone episode during the KORUS-AQ campaign, Atmos. Environ., 224, 117341, https://doi.org/10.1016/j.atmosenv.2020.117341, 2020c.

Souri, A. H., OI-SAT-GMI (0.1.0). Zenodo. https://doi.org/10.5281/zenodo.10520136, 2024

Spivakovsky, C. M., Logan, J. A., Montzka, S. A., Balkanski, Y. J., Foreman-Fowler, M., Jones, D. B. A., Horowitz, L. W., Fusco, A. C., Brenninkmeijer, C. a. M., Prather, M. J., Wofsy, S. C., and McElroy, M. B.: Three-dimensional climatological distribution of tropospheric OH: Update and evaluation, J. Geophys. Res. Atmos., 105, 8931–8980, https://doi.org/10.1029/1999JD901006, 2000.

https://doi.org/10.5194/egusphere-2024-410
Preprint. Discussion started: 29 February 2024

Stavrakou, T., Müller, J.-F., De Smedt, I., Van Roozendael, M., van der Werf, G. R., Giglio, L., and Guenther, A.: Global emissions of non-methane hydrocarbons deduced from SCIAMACHY formaldehyde columns through 2003–2006, Atmos. Chem. Phys., 9, 3663–3679, https://doi.org/10.5194/acp-9-3663-2009, 2009.

Strode, S. A., Duncan, B. N., Yegorova, E. A., Kouatchou, J., Ziemke, J. R., and Douglass, A. R.: Implications of carbon monoxide bias for methane lifetime and atmospheric composition in chemistry climate models, Atmos. Chem. Phys., 15, 11789–11805, https://doi.org/10.5194/acp-15-11789-2015, 2015.

Strode, S. A., Wang, J. S., Manyin, M., Duncan, B., Hossaini, R., Keller, C. A., Michel, S. E., and White, J. W. C.: Strong sensitivity of the isotopic composition of methane to the plausible range of tropospheric chlorine, Atmos. Chem. Phys., 20, 8405–8419, https://doi.org/10.5194/acp-20-8405-2020, 2020.

Strode, S. A., Ziemke, J. R., Oman, L. D., Lamsal, L. N., Olsen, M. A., and Liu, J.: Global changes in the diurnal cycle of surface ozone, Atmos. Environ., 199, 323–333, https://doi.org/10.1016/j.atmosenv.2018.11.028, 2019.

Thompson, A. M., Stauffer, R. M., Wargan, K., Witte, J. C., Kollonige, D. E., and Ziemke, J. R.: Regional and Seasonal Trends in Tropical Ozone From SHADOZ Profiles: Reference for Models and Satellite Products, J. Geophys. Res. Atmos., 126, e2021JD034691, https://doi.org/10.1029/2021JD034691, 2021.

Trenberth, K. E., Fasullo, J., and Smith, L.: Trends and variability in column-integrated atmospheric water vapor, Clim. Dyn., 24, 741–758, https://doi.org/10.1007/s00382-005-0017-4, 2005.

Turner, A. J., Frankenberg, C., Wennberg, P. O., and Jacob, D. J.: Ambiguity in the causes for decadal trends in atmospheric methane and hydroxyl, Proc. Natl. Acad. Sci., 114, 5367–5372, https://doi.org/10.1073/pnas.1616020114, 2017.

Valin, L. C., Fiore, A. M., Chance, K., and González Abad, G.: The role of OH production in interpreting the variability of CH2O columns in the southeast U.S., J. Geophys. Res. Atmos, 121, 478–493, https://doi.org/10.1002/2015JD024012, 2016.

van Marle, M. J. E., Kloster, S., Magi, B. I., Marlon, J. R., Daniau, A.-L., Field, R. D., Arneth, A., Forrest, M., Hantson, S., Kehrwald, N. M., Knorr, W., Lasslop, G., Li, F., Mangeon, S., Yue, C., Kaiser, J. W., and van der Werf, G. R.: Historic global biomass burning emissions for CMIP6 (BB4CMIP) based on merging satellite observations with proxies and fire models (1750–2015), Geosci. Model Dev., 10, 3329–3357, https://doi.org/10.5194/gmd-10-3329-2017, 2017.

Vinken, G. C. M., Boersma, K. F., Maasakkers, J. D., Adon, M., and Martin, R. V.: Worldwide biogenic soil NOx emissions inferred from OMI NO2 observations, Atmos. Chem. Phys., 14, 10363–10381, https://doi.org/10.5194/acp-14-10363-2014, 2014.

Wang, R. and Liu, Y.: Recent declines in global water vapor from MODIS products: Artifact or real trend?, Remote Sens. Environ., 247, 111896, https://doi.org/10.1016/j.rse.2020.111896, 2020.

Wang, Y., Lin, N., Li, W., Guenther, A., Lam, J. C. Y., Tai, A. P. K., Potosnak, M. J., and Seco, R.: Satellite-derived constraints on the effect of drought stress on biogenic isoprene emissions in the southeastern US, Atmos. Chem. Phys., 22, 14189–14208, https://doi.org/10.5194/acp-22-14189-2022, 2022.

Wolfe, G. M., Nicely, J. M., St. Clair, J. M., Hanisco, T. F., Liao, J., Oman, L. D., Brune, W. B., Miller, D., Thames, A., González Abad, G., Ryerson, T. B., Thompson, C. R., Peischl, J., McKain, K., Sweeney, C., Wennberg, P. O., Kim, M., Crounse, J. D., Hall, S. R., Ullmann, K., Diskin, G., Bui, P., Chang, C., and Dean-Day, J.: Mapping hydroxyl variability throughout the global remote troposphere via synthesis of airborne and satellite formaldehyde observations, Proc. Natl. Acad. Sci., 116, 11171–11180, https://doi.org/10.1073/pnas.1821661116, 2019.

Yienger, J. J. and Levy II, H.: Empirical model of global soil-biogenic NOχ emissions, J. Geophys. Res. Atmos, 100, 11447–11464, https://doi.org/10.1029/95JD00370, 1995.

Zhang, Q., He, K., and Huo, H.: Cleaning China's air, Nature, 484, 161–162, https://doi.org/10.1038/484161a, 2012.

Zhang, Z., Poulter, B., Feldman, A. F., Ying, Q., Ciais, P., Peng, S., and Li, X.: Recent intensification of wetland methane feedback, Nat. Clim. Chang., 13, 430–433, https://doi.org/10.1038/s41558-023-01629-0, 2023.

https://doi.org/10.5194/egusphere-2024-410
Preprint. Discussion started: 29 February 2024

Zhang, Z., Zimmermann, N. E., Kaplan, J. O., and Poulter, B.: Modeling spatiotemporal dynamics of global wetlands: comprehensive evaluation of a new sub-grid TOPMODEL parameterization and uncertainties, Biogeosciences, 13, 1387–1408, https://doi.org/10.5194/bg-13-1387-2016, 2016.

Zhao, Y., Saunois, M., Bousquet, P., Lin, X., Berchet, A., Hegglin, M. I., Canadell, J. G., Jackson, R. B., Hauglustaine, D. A., Szopa, S., Stavert, A. R., Abraham, N. L., Archibald, A. T., Bekki, S., Deushi, M., Jöckel, P., Josse, B., Kinnison, D., Kirner, O., Marécal, V., O'Connor, F. M., Plummer, D. A., Revell, L. E., Rozanov, E., Stenke, A., Strode, S., Tilmes, S., Dlugokencky, E. J., and Zheng, B.: Inter-model comparison of global hydroxyl radical (OH) distributions and their impact on atmospheric methane over the 2000–2016 period, Atmos. Chem. Phys., 19, 13701–13723, https://doi.org/10.5194/acp-19-13701-2019, 2019.

Zhao, Y., Saunois, M., Bousquet, P., Lin, X., Berchet, A., Hegglin, M. I., Canadell, J. G., Jackson, R. B., Deushi, M., Jöckel, P., Kinnison, D., Kirner, O., Strode, S., Tilmes, S., Dlugokencky, E. J., and Zheng, B.: On the role of trend and variability in the hydroxyl radical (OH) in the global methane budget, Atmos. Chem. Phys., 20, 13011–13022, https://doi.org/10.5194/acp-20-13011-2020, 2020.

Zheng, B., Chevallier, F., Yin, Y., Ciais, P., Fortems-Cheiney, A., Deeter, M. N., Parker, R. J., Wang, Y., Worden, H. M., and Zhao, Y.: Global atmospheric carbon monoxide budget 2000–2017 inferred from multi-species atmospheric inversions, Earth Syst. Sci. Data., 11, 1411–1436, https://doi.org/10.5194/essd-11-1411-2019, 2019.

Zhu, L., Mickley, L. J., Jacob, D. J., Marais, E. A., Sheng, J., Hu, L., Abad, G. G., and Chance, K.: Long-term (2005–2014) trends in formaldehyde (HCHO) columns across North America as seen by the OMI satellite instrument: Evidence of changing emissions of volatile organic compounds, Geophys. Res. Lett., 44, 7079–7086, https://doi.org/10.1002/2017GL073859, 2017.

Zhu, Q., Laughner, J. L., and Cohen, R. C.: Combining Machine Learning and Satellite Observations to Predict Spatial and Temporal Variation of near Surface OH in North American Cities, Environ. Sci. Technol., 56, 7362–7371, https://doi.org/10.1021/acs.est.1c05636, 2022.

Ziemke, J. R., OMI/MLS tropospheric ozone columns, Greenbelt, MD, USA, Accessed: May 2023, https://acd-ext.gsfc.nasa.gov/Data_services/cloud_slice/data/tco_omimls.nc